

Technology Development for Exoplanet Missions

Technology Milestone Final Report

Laboratory Demonstration of High Contrast Using PIAACMC on a Segmented Aperture

Ruslan Belikov (PI), Eduardo Bendek (deputy PI), Dan Sirbu, Eugene Pluzhnik, Stephen Bryson
(NASA Ames Research Center)

Brian Kern (Institutional PI), David Marx, Dan Wilson
(NASA Jet Propulsion Laboratory)

Olivier Guyon, Justin Knight
(The University of Arizona)

November 24, 2024

Approvals

Released by

Ruslan Belikov
Principal Investigator, NASA ARC

Date

Approved by

Brendan Crill
Exoplanet Exploration Program Deputy Chief Technologist, NASA JPL

Date

Nicholas Siegler
Exoplanet Exploration Program Chief Technologist, NASA JPL

Date

Lucas Paganini
Exoplanet Exploration Program Executive, NASA-HQ

Date

Contents

Contents	2
1 Introduction and Background	3
2 Summary of Milestones and Demonstrations	5
2.1 Review of milestone definitions	5
2.2 Summary of results and achievements, vs. milestone metrics	6
3 Milestone 1 demonstration.....	7
3.1 Design process and chosen design.....	7
3.1.1 PIAACMC Design and testing pipeline.....	7
3.1.2 PIAA mirror and ideal PIAACMC design.....	8
3.1.3 Focal plane mask.....	12
3.1.4 Additional suppression by deformable mirror	12
3.2 Milestone 1 certification and data package.....	14
4 Laboratory Demonstrations: Milestones 2 and 3	14
4.1 Hardware and layout	14
4.2 Calibrations	17
4.2.1 Wavefront Error and Flattening.....	17
4.2.2 CMC Alignment.....	19
4.2.3 Lyot Mask Alignment.....	20
4.2.4 Source Alignment (Upstream Tip/Tilt/Focus).....	20
4.2.5 Back-end Focus.....	21
4.2.6 DM Registration.....	22
4.2.7 Photometry.....	22
4.3 Laboratory results and milestone certification data package.....	22
4.3.1 Summary of performance against milestone metrics.....	22
4.3.2 Calibrated Images of the coronagraph transmittance profile (item #2 in certification data package).....	25
4.3.3 Calibrated Images & Residual Light in the Dark Zone (items #3-5 in the certification data package).....	26
4.3.4 Drift.....	34
4.4 Tip-tilt sensitivity measurements	35
4.4.1 Tip-Tilt Sensitivity.....	35
4.4.2 Coronagraph Jitter Sensitivity.....	36
4.5 Preliminary analysis of limiting factors	38
5 Conclusions.....	39
6 Acknowledgements.....	39
References and Citations.....	41
7 List of Acronyms	44

1 Introduction and Background

Direct imaging of planets, and especially Earth-like planets, is an important goal of exoplanet science and is one of the top recommendations of the Astro2020 decadal survey (<https://doi.org/10.17226/26141>). It is also the driving science goal of Astro2020-recommended Habitable Worlds Observatory flagship. Although a direct image of an Earth-like planet around the nearest stars can in theory be accomplished with very small monolithic apertures as small as 0.45cm (Belikov et al. 2015), much larger, likely segmented mirrors are needed to do a survey for potentially habitable planets around dozens or hundreds of nearby stars. NASA’s flagship studies LUVOIR (Fischer et al., 2019) and HabEx (Gaudi, Seager, et al., 2019) described point designs to conduct such a survey. The LUVOIR concept had two options: LUVOIR A is based on a 15m on-axis segmented aperture with a central obstruction and spiders (Figure 1, left); and LUVOIR B is based on an 8m off-axis segmented aperture (Figure 1, right). In addition, the HabEx mission evaluated several segmented aperture options, but baselined a monolithic aperture, in part due to the perceived challenges of high performance coronagraphs on segmented apertures.

Astro2020 suggested a 6m off-axis telescope as a baseline, but it is important to note that both the size, and whether the telescope is on-axis or off-axis, are still subject to trade. In particular, the motivation for an off-axis architecture has mostly to do with the fact that current coronagraph designs for off-axis apertures perform better in the lab than for on-axis apertures. However, this performance gap is probably due to technological maturity and not due to fundamental physics (Belikov et al., 2021). In other words, with sufficient engineering, coronagraphs on on-axis apertures should have comparable performance to off-axis apertures. (More generally, physics-limited coronagraph performance is only weakly dependent on telescope aperture shape.) On-axis apertures have significant advantages for flagships: they are mechanically simpler, less risky, and are lower cost; they require smaller and lower cost sun-shields; and allow larger apertures for the same mass, volume, and/or price.

Furthermore, a key theme running through Astro2020 as well as several other studies of flagship missions (SMD Large mission study; Bitten et al, 2021) is that better and more thorough early trades and technology development are needed to lower the risk and cost of flagship missions. A good way of achieving this is more efficient and/or robust coronagraphic instruments. In theory, the Earth-like exoplanet yield of coronagraphs on a flagship mission can be improved by a factor of ~2-4 for off-axis and on-axis designs, respectively, simply by improving coronagraph efficiency and robustness to instabilities, for a given spectral band and quantum efficiency (Belikov et al., 2021), and even more if spectral band and QE can be improved. Such improvements in performance reduce many key risks and costs: the risk of η_{\oplus} being low, the risk and cost associated with building an ultra-stable telescope, and the cost of a larger aperture. (Yield goes roughly as 2nd or 3rd power of telescope diameter (Stark et al., 2019), so that a factor of 4 improvement in yield can be equivalent to doubling the telescope aperture.)

It is not clear what coronagraph technologies can best improve the current state of the art and bring us closer to physics-limited performance, but the Phase Induced Amplitude Apodization (PIAA, Guyon et al., 2003) family of coronagraphs is one promising path. PIAA achieves high level of starlight suppression by using two aspheric mirrors to apodize the pupil of the telescope. For the case of the “classical” PIAA coronagraph, this apodization suppresses the Airy diffraction rings of a stellar point spread function, revealing the star’s planetary system. Classic PIAA provides high performance coronagraph designs for monolithic apertures. In this work, we have been developing a variant called PIAACMC (PIAA Complex-valued Mask Coronagraph (Guyon

et al., 2010, 2013), which allows high performance on obstructed (and more generally, arbitrarily shaped) apertures. Similarly to PIAA, PIAACMC includes two aspheric mirrors which apodize the pupil. However, in addition to these two mirrors, PIAACMC also employs a partially transmissive pi-phase shifting mask. In practice, such an “ideal” mask is implemented by a fully reflective holographic mask, which emulates the far-field response of the ideal CMC mask. In theory, the PIAACMC coronagraph with an ideal CMC mask and no manufacturing errors is capable of fully suppressing an on-axis point source for any arbitrary aperture in broadband light. (Practical implementations of the CMC mask may never reach this ideal, but with sufficient engineering, they can come arbitrarily close.)

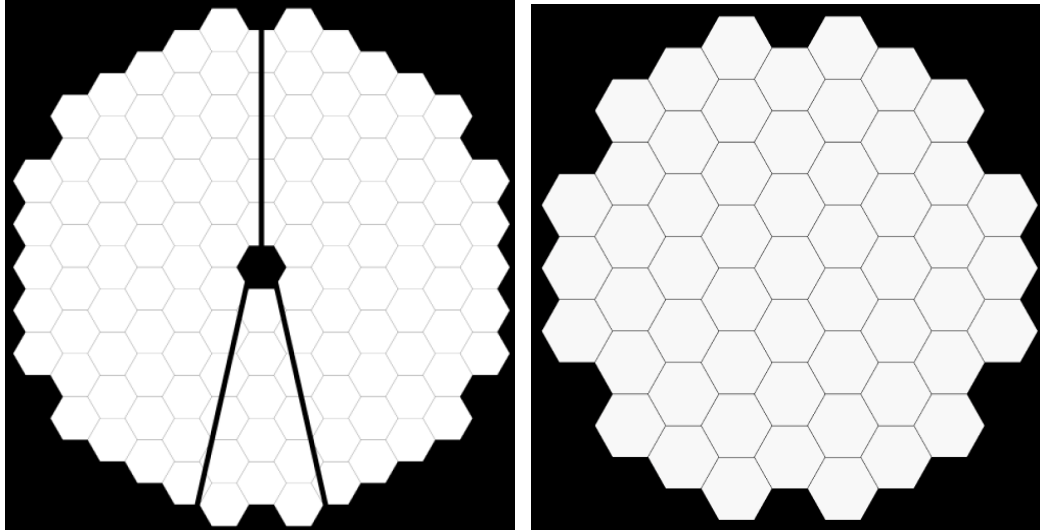


Figure 1.Left: LUVOIR A aperture (15m circumscribed diameter). Right: LUVOIR B aperture (8m circumscribed diameter). This report describes tests for the (more challenging) LUVOIR A aperture.

However, a key practical challenge for coronagraphs is sensitivity to stellar angular sizes, or equivalently, tip-tilt jitter of the telescope. For the case of the LUVOIR telescope, for example, some of the target stars have angular diameters on the order of $0.1 \lambda/D$. Thus, a coronagraph design for such a telescope needs to suppress starlight for the case that a star is a disk (of mutually incoherent light) with $\sim 0.1 \lambda/D$ diameter. In theory, there is a fundamental trade-off between inner working angle and sensitivity to stellar angular size, which applies not just to PIAA, but to all coronagraphs as a whole (Belikov et al., 2021). In particular, coronagraphs with inner working angles of $\sim 1 \lambda/D$ or less will not be able to achieve good stellar suppression in the presence of stars with $0.1 \lambda/D$ angular diameters. Fortunately, relaxing the inner working angle to 2 or 3 λ/D allows very deep suppression of such stars, although finding a design that achieves this for a particular coronagraph architecture can still be challenging.

For the case of monolithic apertures, the sensitivity to stellar angular size steadily improves as the inner working angle gets larger, both for PIAA and PIAACMC (Guyon et al. 2010). Therefore, coronagraph designs can readily be found for any desired stellar angular size, at the expense of the inner working angle. In addition, coronagraphs on segmented apertures (such as LUVOIR B) appear to perform similarly to monolithic apertures, because modern wavefront control systems appear to be able to mitigate the effects of segmentation, for many coronagraph architectures.

For the case of obstructed apertures, PIAACMC sensitivity to stellar angular size does not steadily improve with inner working angle, and in fact sometimes degrades. Nevertheless our

PIAACMC design for LUVOIR A is tolerant to at least $\sim 0.01 \lambda/D$ stellar angular diameter and was described in detail in (Belikov et al. 2018). This design improves LUVOIR A baseline yield from 47 to 51, based on simulations with the Altruistic Yield Optimizer (Stark et al. 2015) that modeled several coronagraphic instruments on the flagship working in tandem, choosing different ones for different targets. To be more precise, the best combination of coronagraphs involving PIAACMC have yield of 51, while the best combinations that do not have 47. Although these improvements fall short of the factor of 2-4 theoretical potential, further improvements are possible since we have not yet exhausted the design space. (In particular, one promising path is the hybrid PIAA-vortex coronagraph (Fogarty et al. 2022)). In addition, our design enables targets that are not otherwise accessible, such as stars that are farther away and/or more later type stars such as K-dwarfs. Finally, our PIAA design for LUVOIR B is tolerant to $0.1 \lambda/D$ stellar angular diameter, and improves yield from 28 to 42. However, this work focused on testing of our LUVOIR A design in order to advance coronagraphic performance for the more challenging case: obstructed apertures.

Note that this section was intended as a very brief overview. Please see the original white paper for a more comprehensive overview of the background and motivation for this project.

2 Summary of Milestones and Demonstrations

2.1 Review of milestone definitions

Milestone 1 (July 13, 2018). *Demonstration of an end-to-end computer simulation of proposed HCIT-2 layouts, with the new PIAACMC design and wavefront control, that reaches the following performance: $1e-9$ raw contrast averaged between 2 and $8 \lambda/D$, under the following conditions:*

- (a) *in a 10% wavelength band (baseline center wavelength 650nm);*
- (b) *in one polarization (polarized source and analyzer in front of science focal plane);*
- (c) *for the version of the LUVOIR pupil as specified by STDT as of Dec 2017;*
- (d) *tip/tilt jitter of $0.004 \lambda/D$ rms per axis.*

Milestone 2. (Dec 10, 2019) *Laboratory demonstration of $1e-9$ raw contrast averaged between 2 and $8 \lambda/D$, under the following conditions:*

- (a) *in monochromatic light (baseline wavelength 650nm);*
- (b) *in one polarization (polarized source and analyzer in front of science focal plane);*
- (c) *for the version of the LUVOIR pupil as specified by STDT as of Dec 2017;*
- (d) *assuming that level of tip/tilt error on HCIT is $< 0.004 \lambda/D$ rms per axis. This level of error will either be confirmed in year one, or milestone will be rewritten to correspond to actual testbed jitter.*

Milestone 3. (Dec 18, 2020) *Same as milestone 2, but in broadband light. Specifically, laboratory demonstration of $1e-9$ raw contrast averaged between 2 and $8 \lambda/D$, under the following conditions:*

- (a) *in a 10% wavelength band (baseline center wavelength 650nm);*
- (b) *in one polarization (polarized source and analyzer in front of science focal plane);*
- (c) *for the version of the LUVOIR pupil as specified by STDT as of Dec 2017;*

(d) assuming that level of tip/tilt error on HCIT is $< 0.004 \lambda/D$ rms per axis. This level of error will either be confirmed in year one, or milestone will be rewritten to correspond to actual testbed jitter.

2.2 Summary of results and achievements, vs. milestone metrics

Table 1. Milestone status summary.

Milestone	Primary Technical Metrics	Requirement	Demonstrated Performance		Status
			inner region	outer region	
1. PIAACMC design and end-to-end computer model validation.	Mean contrast	1e-9	9e-10	5.6e-10	Successfully completed (with some margin in all 3 parameters)
	Dark Zone (and IWA w/o field stop)	2-8 λ/D (2 λ/D)	2-4 (1.4 λ/D)	4-8 (1.4 λ/D)	
	Tip/tilt tolerance ² per axis (rms)	4e-3 λ/D	5e-3 λ/D		
2. Lab demo, monochromatic light	Mean contrast	1e-9	1.1e-7 (4.1e-8 modulated)	9e-9 (1.6e-9 modulated)	Requirement not met (but, record performance achieved for obstructed segmented aperture ³)
	Dark Zone (and IWA ¹ w/o field stop)	2-8 λ/D (2 λ/D)	2-4 λ/D (1.4 λ/D)	4-8 λ/D (1.4 λ/D)	IWA ¹ requirement exceeded by 30%
	Tip/tilt tolerance ² per axis (rms)	4e-3 λ/D	5e-3 λ/D		tolerance requirement exceeded by ~25%
3. Lab demo, 10% broadband light	Mean contrast:	1e-9	Not tested	1.9e-8 (9e-9 modulated)	Requirement not met (but, record performance achieved for obstructed segmented aperture ³)
	Dark Zone (and IWA ¹ w/o field stop)	2-8 λ/D (2 λ/D)	2-3.5 λ/D (1.4 λ/D)	3.5-8 λ/D (1.4 λ/D)	IWA ¹ requirement exceeded by 30%
	Tip/tilt tolerance ² per axis (rms)	4e-3 λ/D	5e-3 λ/D		tolerance requirement exceeded by ~25%

¹ IWA represents potential IWA if a larger field stop is used – otherwise IWA is defined by stated dark zone edge

² tip/tilt tolerance refers to the amount for which total contrast degrades to 1e-9 contrast for a circularly symmetrical Gaussian jitter with the stated rms per axis. A star with radius equal to twice that value will have the same mean contrast, for a 2nd order coronagraph and no limb darkening, i.e. our design is tolerant to $\sim 0.02 \lambda/D$ diameter stars

³To our best knowledge: (a) our work represents the only demonstrations of high contrast in vacuum for an obstructed segmented aperture; (b) record lab performance for *off-axis* segmented apertures is 4.7e-9, 3-10 λ/D , 10% band (Vector Vortex, Riggs et al. 2022); (c) on-axis monolithic aperture: 1.6e-9, 3-9 λ/D , 10% band (Hybrid Lyot, Seo et al. 2017); (d) off-axis monolithic aperture: 4e-10, 3-8 λ/D , 10% band (Classical Lyot, Seo et al. 2019).

A summary of our results, compared to primary milestone metrics, is shown in Table 1. (Technical details behind these results will be covered in sections 3-4.) Table cells colored in green refer to results that successfully meet milestone metrics; yellow cells represent results that have not met the milestone metrics but nevertheless represented a significant advance beyond the state of the art for lab demonstrations with segmented and obstructed pupils. The orange cell represents an aspect that was not tested.

The “modulated” results refer to contrast of the component of the speckle field that is coherent with respect to the star (i.e. whose electric field can be “modulated” – see a more precise definition in section 4.3.1.) The significance of the “modulated” metric is that it reflects the contrast that can be achieved if all sources of incoherent light were to be removed (either by better baffling or subtracting in software, since incoherent light is usually static).

Although not all milestones were fully met, this work does advance the state of the art in the following ways. First, yield simulations that were solely based on, or included our designs were able to achieve the best yields for LUVOIR B and LUVOIR A, out of all coronagraph designs studied with the Altruistic Yield Optimizer (Stark et al. 2019). Second, our lab demonstrations represent, to our best knowledge, the best results ever achieved with an obstructed and segmented aperture (though may soon be surpassed by HiCAT results with the APLC, at least in terms of contrast). Finally, they represent the best tolerance to tip/tilt out of all PIAA demonstrations to date.

3 Milestone 1 demonstration

3.1 Design process and chosen design

3.1.1 PIAACMC Design and testing pipeline

Our design and test pipeline is diagramed in Figure 2. For most of our design and simulations, we used a simplified "compact" layout where several components are assumed to be in the same plane and all components are assumed to be the same size. In the real setup (Figure 9) there are reimaging optics, and not all optics are the same size. However, the compact design abstracts this away for simplicity, because these details usually do not affect the design of the coronagraph components themselves. A compact design can be converted into a real layout without changing design of components as long as the Fresnel number of each component stays the same.

We used two methods to propagate between PIAA optics, depending on the approximation level and computational speed required for a particular task: simple geometrical remapping (i.e. the limit of infinitely small wavelengths, or ray optics), or Fresnel diffraction propagation (treating the PIAA optics as infinitely thin plates which impose an optical path delay that is a function of the lateral coordinates). The propagation between PIAA2+DM plane was implemented by a convolution between the electric field immediately after the PIAA+DM plane and the Fourier Transform of the Focal Plane mask. The focal plane mask itself in general has the form of some complex-valued transmission $M(x, y)$, or $M(r, \theta)$ in polar coordinates. Beyond some value $r > R_{mask}$, the mask is fully transmissive, i.e. $M(r, \theta) = 1$. In order to numerically model such a mask with finite-sized arrays, we used a standard technique based on Babinet's principle, where instead

of using the actual M as our mask, we used $M' = M - I$, and then applied a correction in the Lyot plane (adding the electric field corresponding to the case $M = I$). This allowed representing the mask transmission by an array sampled on a grid going out only to R_{mask} , which saved significant memory and computational speed.

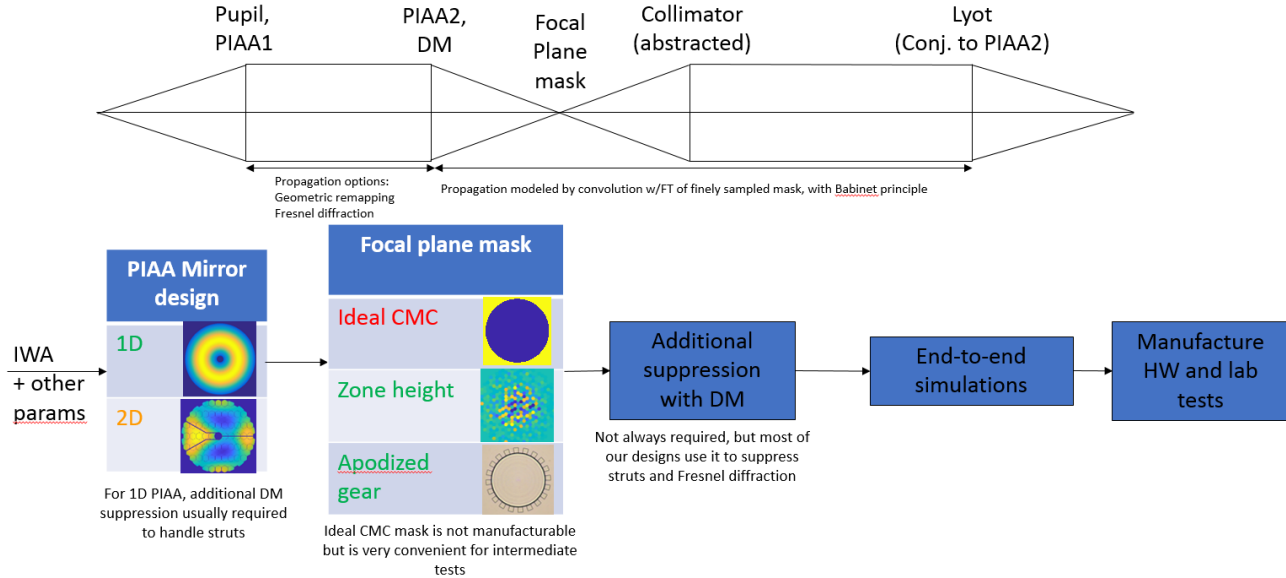


Figure 2. Design and testing pipeline. Top: simplified diagram of the PIAA layout used for designing PIAACMC components (PIAA mirrors, CMC mask, Lyot stop). Bottom: Design work flow. PIAA mirrors are designed first, then the focal plane mask, followed by additional suppression by the deformable mirror.

We explored several design strategies for PIAA mirrors and focal plane mask. A key branching point was whether to design a coronagraph (PIAA optics and mask) for a 1D pupil, i.e. a pupil as a function of radius only, which includes the central obstruction but not segments or struts, or for a full 2D pupil. For the case of a coronagraph designed for a 1D pupil, additional suppression with a DM was required to suppress light leaked from struts and segments. As long as the struts and segments are sufficiently thin, this usually resulted in a realistic (i.e. achievable) shape on the DM. It turns out that the LUVOIR pupil struts and segments are indeed sufficiently thin for the DM to suppress them (as will be shown in section 3.1.4), and so we focused our design efforts of the PIAA optics for a 1D pupil.

After PIAA mirrors were designed, the next step was to design a focal plane mask. We considered three options: an ideal "Complex-valued Mask for Coronagraphs" (ideal CMC) which achieves full coronagraphic suppression in broadband light (Guyon et al., 2014) but is not manufacturable with current technologies. (So-called "zone height" masks are manufacturable but are computationally intensive to design; and "apodized gear" masks are less computationally intensive to design but are less mature than the zone height masks.) In this report, we focus on a design based on the zone height masks, and will cover masks in more detail in Section 3.1.3.

After the PIAA mirrors and masks were designed for an obstructed 1D pupil, we inserted the full 2D pupil (i.e. struts and segment gaps), and computed a surface on the deformable mirror that suppresses the light leak from struts and segment gaps, as described in section 3.1.4.

3.1.2 PIAA mirror and ideal PIAACMC design

Our PIAA mirror design methods were based on Guyon et al. 2010, Soummer et al. 2004, and Belikov et al. 2006. In this step of the process, we essentially computed an ideal PIAACMC coronagraph (Guyon et al. 2010) for the compact layout in Figure 2. An ideal PIAACMC involves two idealizations: (1) there is no diffraction propagation between the two PIAA mirrors, so that the propagation is purely geometric; (2) the mask is the "ideal CMC", which is a simple 2-zone mask, where the transmission is some value $-t$ inside mask radius q_0 , and 1 otherwise. The value of t is some constant between 0 and 1, depending on the mask radius q_0 , so that the inside of the mask imposes an achromatic partially transmissive pi-phase shift. The Lyot stop in the ideal coronagraph is identical to the pupil.

Ideal PIAACMC coronagraphs achieve full coronagraphic suppression of on-axis sources for arbitrarily obstructed pupils in broadband light. For any given pupil apertures at PIAA1 and PIAA2 planes, there is a continuous family of PIAACMC designs parametrized by mask radius q_0 , or equivalently the inner working angle of the coronagraph, which is monotonically related to q_0 . This relationship is shown in Figure 4, for the case where the pupil apertures at PIAA1 and PIAA2 are both circular apertures with a 10% obstruction in the middle. All designs in this section have this pair of apertures at PIAA1 and PIAA2. The inner working angle is defined as the off-axis angle of a point source in the sky, in λ/D units, at which the total energy transmitted to the final science plane is $\frac{1}{2}$ of the total energy immediately after the entrance pupil. Inner working angles can be as small as $\sim 0.5 \lambda/D$, but larger inner working angles result in coronagraphs that are more tolerant to tip/tilt errors and angular stellar sizes. The q_0 parameter values are listed in "system λ/D units", which essentially treat PIAA2 plane as the pupil of the system instead of PIAA1. Hence, the relation between on-sky λ/D units and system λ/D units is the effective magnification induced by the two PIAA optics, because remapping between PIAA1 and PIAA2 changes the effective diameter of the pupil.

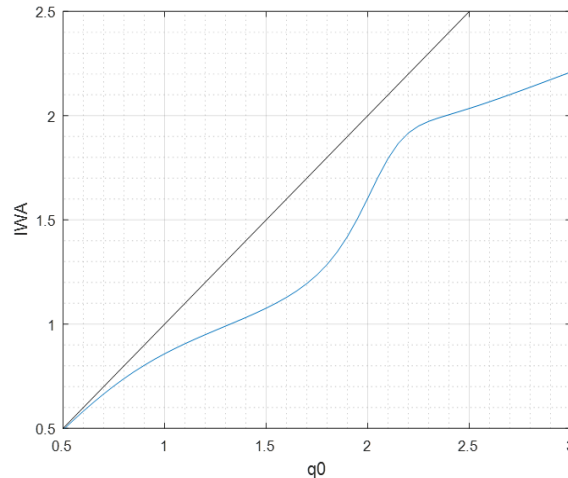


Figure 3. Relationship between the mask radius q_0 (in λ/D system units), and the inner working angle of the system, in blue color. The black line is $IWA = q_0$, shown simply for reference, corresponding to the case of no magnification.

In Figure 4, we show two selected points from the continuous family of PIAACMC designs, corresponding to $q_0 = 2.6$ and 1.9 , respectively (inner working angles of 2.07 and $1.4 \lambda/D$). As q_0 increases, the apodization and PIAA shapes change from monotonic ones (such as the one on the bottom of Figure 4) where the only extrema are on the inner and outer edges of the aperture, to "donut" shapes, where there is an extremum between the aperture edges. Figure 5 also shows how

the geometric propagation idealization (red curve) compares to Fresnel diffraction (blue curve), for the case of 36mm diameter optics separated by 40cm. Fresnel diffraction causes a contrast degradation from 0 (full suppression) to $\sim 1e-7$ in this case, which we note here but defer a more detailed discussion till section 3.1.4, where we show that a deformable mirror can be used to suppress residual light due to Fresnel diffraction.

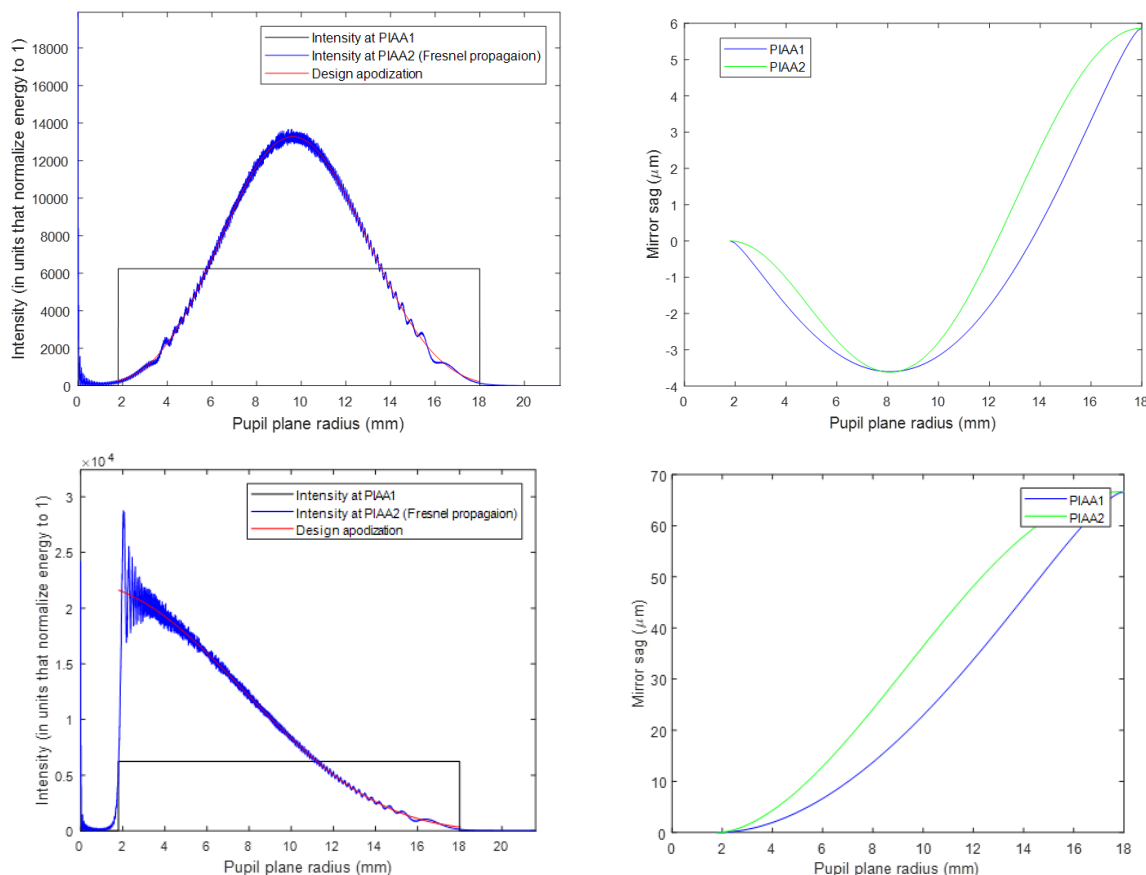


Figure 4. Examples of 1D PIAA apodizations and resulting PIAA mirror shapes. Top and bottom rows corresponds to PIAA apodizations for $q_0=2.6$, and $1.9 \lambda/D$ in system units, respectively. Left column shows the original intensity at the pupil before PIAA, the design apodization, and the Fresnel-propagated apodization. The right column shows the PIAA mirror sags which reproduce the design apodization in the geometrical optics limit.

We also studied the sensitivity of ideal PIAACMC designs to tip/tilt, as well as two different variations of the ideal PIAACMC focal plane mask. Ideal PIAACMC designs appear to have a second-order sensitivity to tip/tilt modes, which is to say that the energy of the residual starlight in the final science plane grows as the amplitude of tip/tilt mode to the second power, for small tip/tilts. Figure 6 shows raw contrast of the residual light in the science plane, averaged between 2 and 8 λ/D (in sky units), for different PIAACMC designs, and 0.004 λ/D off-axis point source (thick curves) as well as on-axis point source (thin curves). The black and green curves represent ideal PIAACMC designs (each point on the x-axis represents a different design). Black curve shows the case of an unobstructed pupil while green is the case of the 10% obstructed pupil. In both cases, an on-axis point source is fully suppressed, and the thin black and green curves would be identically 0 if there was no numerical computation error (as it is, the black thin curve is off the

scale and thin green curve is $< 10^{-10}$ contrast). Both curves exhibit the expected trend that coronagraphs with a larger IWA tend to be more tolerant to tip/tilt errors (and stellar angular sizes), except that for the case of the obstructed pupil, designs with IWAs between about 1.4 and $2.0 \lambda/D$ actually have the reverse trend. This tolerance can be improved by varying the remapped obstruction diameter at PIAA2, but was outside the scope of this work. Based on this plot, however, we selected $IWA = 1.4$ as the point design to use for the design of manufacturable masks (section 3.1.3).

Although the green curve in Figure 5 (ideal PIAACMC design) shows good tolerance to tip/tilt, especially for $IWA = 1.4$, the ideal CMC mask is challenging to manufacture because it requires an achromatic pi phase shift, and a mask radius that is proportional to wavelength. The blue and red curves represent more manufacturable masks (for ideal PIAA mirrors with a 10% obstructed pupil), which address the achromatic pi phase shift but not the size-scaling. The blue curve is an "ideal opaque mask", which is the same as the ideal CMC mask, except that it has 0 transmission instead of $-t$. It is a good solution for IWAs $> 2 \lambda/D$, where it converges to the ideal PIAACMC design because the ideal CMC mask transmission asymptotes to 0 as IWA grows. However, it has a poor performance for $IWA < 2 \lambda/D$, where the partial transmission of the ideal CMC mask is needed for good performance. The red curve represents a mask which has a partially transmissive sag (optical path difference) which corresponds to a pi phase shift for the central wavelength. It is thus identical to the ideal CMC mask for the central wavelength, but imposes a slightly different phase shift for off-center wavelengths. It has much better performance than the ideal opaque mask, but still not as good as the ideal CMC mask.

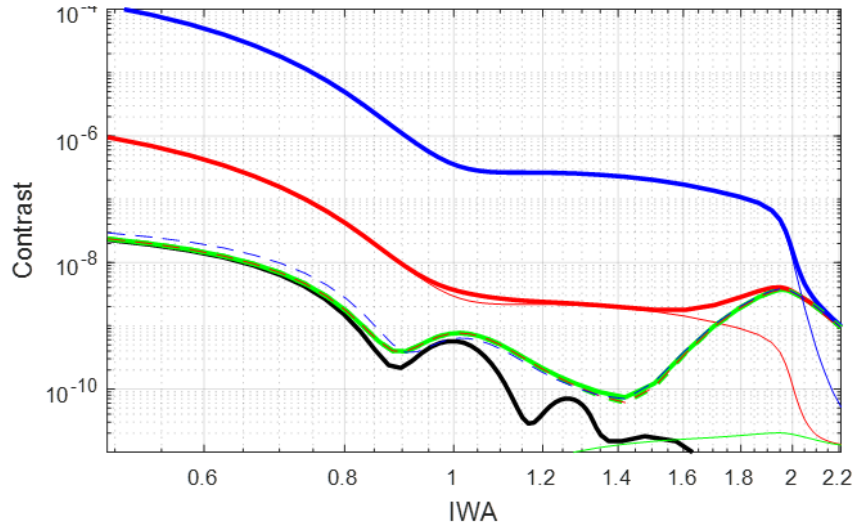


Figure 5. Average raw contrast between 2 and $8 \lambda/D$ on the sky for different ideal or quasi-ideal PIAACMC designs, in a 10% band ($\Delta\lambda/\lambda$). Every point on the x-axis represents a different PIAA apodization and PIAA mirror pair, parametrized by IWA. Black curve is the case of an unobstructed pupil and ideal CMC mask; colored curves are for a 10% obstructed pupil and different masks: green is the ideal CMC, blue is the ideal opaque occulter, and red is the ideal monochromatic occulter. Thin curves represent the case of an on-axis point sources and thick lines represent an off-axis source at $0.004 \lambda/D$ on sky.

The masks represented by the blue and red curves address the practical implementation of the achromatic pi phase shift, but not the scaling of the mask with wavelength. However, they do form interesting starting points for further mask design.

3.1.3 Focal plane mask

We explored several design methodologies for a focal plane mask, as well as for different PIAA mirror designs and pupils. In this report, we focus on the description of the methodology and design we selected for manufacture. Specifically, we used a PIAA apodization from Section 3 for $IWA = 1.4 \lambda/D$ ($q_0 = 1.9$), and 1D pupil apertures that have a 10% obstruction in the PIAA1, PIAA2, and Lyot stop planes. We then replaced the ideal PIAACMC mask by a "zone height mask" and used nonlinear optimization to solve for it.

The zone height mask we selected for manufacture (see Figure 6) is similar to the one developed for the WFIRST PIAACMC design (Kern et al, 2015). It is essentially a reflective hologram, or a mirror with a sag with a finely structured pattern, that consists of hexagonal zones at different heights.

To design the mask, we formulated an optimization problem and used a nonlinear optimization method called differential evolution to solve it, as part of a new coronagraph optimization package we developed called csim. The optimization problem had a predefined optical layout (Figure 2), PIAA apodization as described above, and a predefined geometry of hexagonal zones (number of zones, their size, etc.). Its optimization variables were the heights (sags) of the hexagonal zones, and the objective function was the contrast between 2 and 8 λ/D on the sky, in the presence of three off-axis sources, for a 10% band around 650nm. We let the optimization run until it achieved better than 10^{-9} contrast.

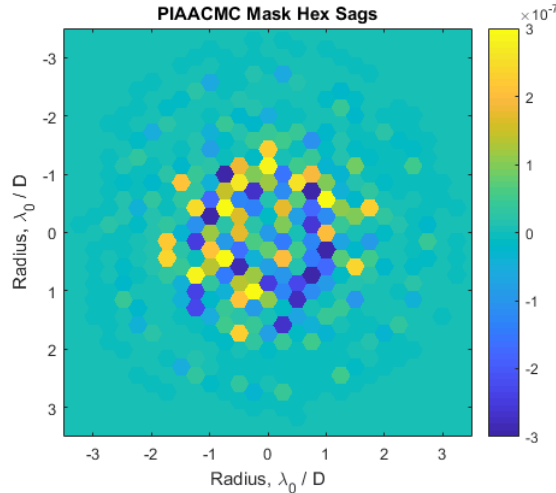


Figure 6. CMC design selected for manufacture. Z-scale in meters.

This produced a design that is manufacturable, and achieves 10^{-9} contrast (between 2 and 8 λ/D on the sky) with a pupil that has only a central obstruction (no struts or segments). Replacing this pupil by a LUVOIR pupil degrades the residual light in the science plane to $\sim 3 \times 10^{-6}$, but it turns out that this residual is correctable in broadband by a deformable mirror.

3.1.4 Additional suppression by deformable mirror

Deformable mirrors can also be the only coronagraphic component in the system, suppressing Airy rings as if they were speckles due to random errors. Used this way, they become equivalent to the "phase mask coronagraph", where the DM functions as a reconfigurable phase mask. However, it is challenging to achieve a high combination of throughput, bandwidth, inner working angle, and Strehl with a pure phase mask coronagraph. Therefore, for our design, we use the DM

only as a support element to remove the perturbing effects of struts and segments, rather than as a primary element.

Figure 7 shows the results of applying EFC to our PIAACMC design, which is the same as in Section 3.1.3, except we inserted the LUVVOIR pupil, performed full diffraction propagations, and used conservative apertures and Lyot stop to reduce Fresnel effects, which reduced throughput from 100% for the ideal case to 74.9% (measured as the ratio of total energy between the entrance and exit pupils, for the case of no occulter). Some or even most of this throughput loss can potentially be recovered by using less conservative apertures, but we judged this throughput and design to be good enough to manufacture.

The specifics of our EFC run were motivated primarily by modeling the test configuration and requirements of our lab layout. Thus, our DM had 32x32 actuators, to match the 1K device by Boston Micromachines, and our dark zone was single-sided rather than double-sided, testing a more conservative configuration consisting of 1DMs rather than 2DMs. (2DMs are usually needed to produce a double-sided dark zone, which adds an orthogonal dimension of complexity and is outside the scope of this work.) We also used a dark zone that has an inner edge of $2 \lambda/D$, rather than $1.4 \lambda/D$, per requirements of our laboratory demo. We have not yet explored more aggressive inner working angles with an EFC solution for this design, but no known limits to this exist, other than the $1.4 \lambda/D$ (soft) limit imposed by the original coronagraph design.

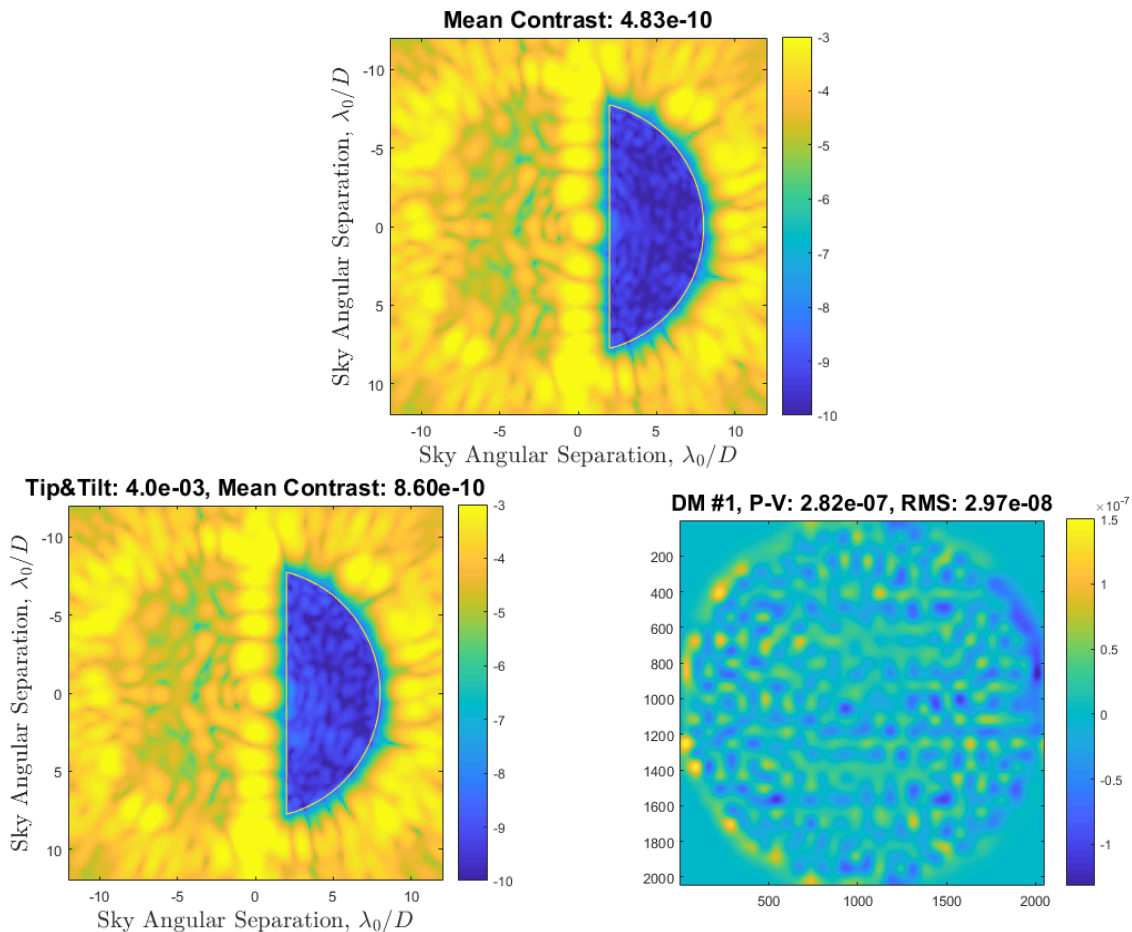


Figure 7. Top: Focal plane contrast in the focal plane with our PIAACMC design for the LUVVOIR pupil. (Top: on-axis source only; Bottom left: two off-axis sources at $4 \times 10^{-3} \lambda/D$). Bottom right: the surface of our deformable mirror that generated these contrast maps. shown is the sag of the DM in units of meters.

3.2 Milestone 1 certification and data package

The results in Figure 7 represent broadband simulations with a bandwidth of 10%, and a dark zone that has an inner edge at $2 \lambda/D$ and an outer diameter of $8 \lambda/D$ (on the sky). For a point source, our contrast was 4.83×10^{-10} (raw speckle intensity averaged across the dark zone), and for two point sources separated by $4 \times 10^{-3} \lambda/D$, the contrast was 8.6×10^{-10} . For a second order coronagraph, the contrast of a tipped or tilted point source also is approximately the same as the contrast for a Gaussian-distributed tip/tilt error (Belikov et al. 2021), with a standard deviation equal to the off-axis displacement of the point source. So, the contrast values for individual off-axis sources can also be interpreted as contrast values for a Gaussian-distributed jitter with the root-mean-square value equal to the off-axis amount of the point source.

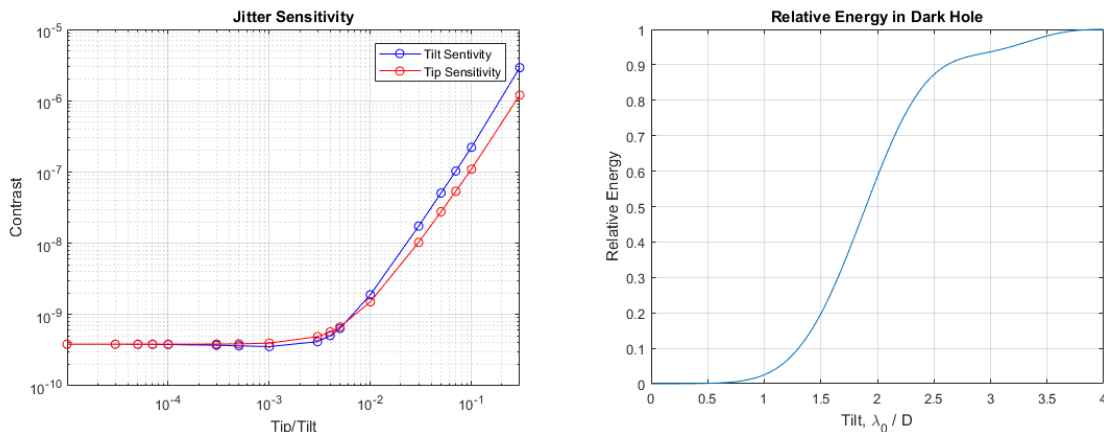


Figure 8. Left: Jitter sensitivity as a function of tip and tilt. Right: Total energy in the dark zone, normalized to the middle of the dark zone. We define the inner working angle as the 50% point of this curve, which is $1.8 \lambda/D$.

The surface of the deformable mirror which yielded these high contrast results is shown on the bottom right of Figure 7. The total sag is less than 300nm, well within the stroke range of most deformable mirrors, and small enough that the Strehl ratio of planets is not degraded significantly (Strehl relative to the PSF of a flat DM was 0.83). In addition, we halted the EFC run before it asymptoted, so that deeper contrasts than what is shown in Figure 8 are possible. However, beyond a certain point, deeper contrasts with EFC come at the expense of greater DM strokes and worsened Strehl.

4 Laboratory Demonstrations: Milestones 2 and 3

4.1 Hardware and layout

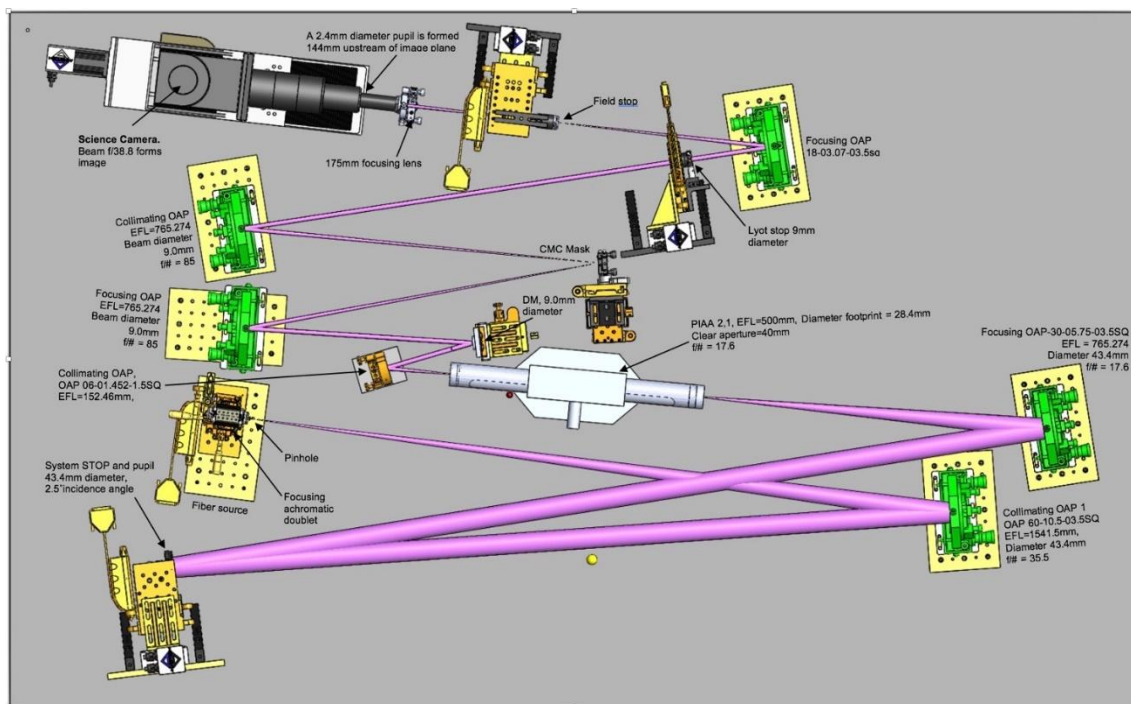
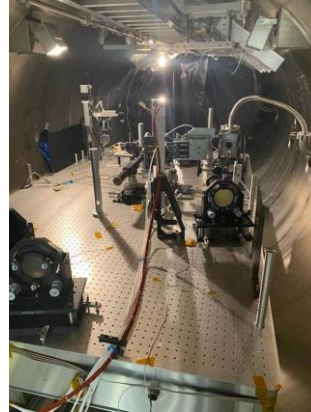
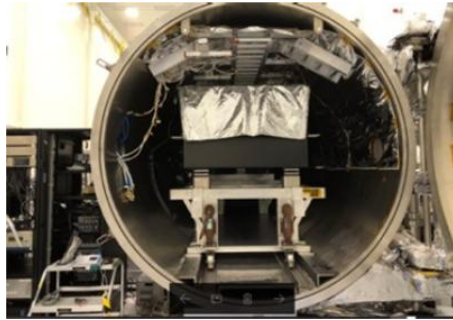
Our prior publications provide detailed coverage of our PIAACMC design (Belikov et al. 2019), modeling (Sirbu et al. 2021), as well as testing procedures and initial results (Marx et al. 2021), which we briefly review here.

The PIAACMC design we manufactured and tested is similar to the one for the mission with one key difference – we optimized the testbed design for a one-sided (180°) dark zone rather than the full double-sided (360°) one. This was done because it allowed for testing with one deformable

mirror rather than two, which served to simplify the system and better isolate the key items we were testing for (contrast in the dark zone and robustness to low order aberrations, which are not strongly dependent on whether one or two DMs are used, according to models). This design achieves $4.83\text{e-}10$ raw contrast in simulation between 2 and 8 λ/D in a 10% band for a point sources, and stays below $1\text{e-}9$ for up to $0.02 \lambda/D$ diameter stars, representing significantly improved tolerance to stellar diameter than prior PIAA designs. A combination of CMC mask and DM were tuned to provide high contrast for a dark zone between 2 and 8 λ/D , but this PIAA mirror design allows IWAs as small as $1.4 \lambda/D$ (with a different CMC and DM shapes, though this would make it more sensitive to tip/tilt and stellar size). We have not fully explored the trade space of this architecture and in particular, designs with contrasts $< 1\text{e-}10$ are possible (with a less aggressive inner working angle or tolerance to aberrations), but we settled on this design as having a good combination of performance parameters for testing at HCIT.

Our tests were conducted at the High Contrast Imaging Testbed (HCIT) facility at NASA JPL, but due to the fact that PIAA layout is not readily compatible with existing HCIT testbeds such as DST, we created an entirely new testbed for our project, shown schematically in Figure 9. Key components of the layout are as follows. First, a single mode fiber and a pinhole serve as a point source of light representing a star, with monochromatic as well as broadband laser options available. This light is then relayed to a pupil mask representing the LUVUOIR A pupil (manufactured by Lambda Consulting using carbon nanotube technology). Light is next relayed to a PIAA system (by NuTek), consisting of a tube with two PIAA mirrors with a hole in the middle corresponding to the pupil obstruction, allowing entry and exit of the light beam. A Boston Micromachines Corporation Kilo-DM with 952 actuators is conjugated to the downstream PIAA mirror (PIAA2) and performs wavefront control. Finally, a CMC mask (by NASA JPL MDL), Lyot stop (by Lambda Consulting), and field stop complete the coronagraphic setup. The final camera can move along the z-axis, covering the range from focus to pupil-conjugate. A polarizer (analyzer) was also placed in front of the camera to isolate polarization effects from other limiting factors, although we have not performed detailed tests of whether polarization was a concern in our system.

Initially, we observed significant mismatches between our model and testbed measurements, but after several iterations of hardware and modeling, we achieved a good match [14]. In particular, empirically measured pupil plane and focal plane illumination match, with and without the CMC mask, to within about 10% over the majority of the illuminated region. In addition, our model calibrations relied not only on measurements of the intensities of different planes in different hardware configurations, but also a phase retrieval procedure to estimate the wavefront error in the system (which separately estimated low order errors upstream and downstream of PIAA). Finally, plate scale as well as DM scale and registration were all empirically calibrated and folded into our models of the system and wavefront control algorithms. Our main wavefront control algorithm was standard pair-wise Electric Field Conjugation (EFC, [17]), although we also used our project as an opportunity to try several other techniques (outside the scope of this paper), including classical speckle nulling and experimental self-calibrating control methods.



PIAA M1

PIAAM2

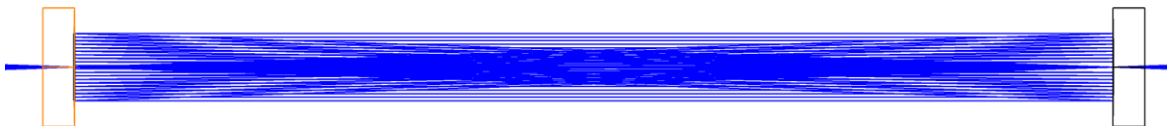


Figure 9 Top: One of the vacuum chambers in the High Contrast Imaging Testbed chamber (HCIT) at NASA JPL (left) and PIAACMC bench (right). **Center:** Test layout of the PIAACMC coronagraph used for the results in this paper. **Bottom:** A raytrace diagram of the PIAA system, showing the inside of the PIAA tube assembly (the white-colored structure in the center image). Light first comes in from the right to the left, focused through the hole of PIAA M2, then diverges to illuminate PIAA M1. PIAAM1 collimates the light as well as imposes the PIAA1 phase. Light then travels to the right to illuminate PIAAM2, which imposes the PIAA2 phase, and converges the light to pass through the hole in PIAA M1.

4.2 Calibrations

A number of calibrations were required prior to EFC. These are shown as a workflow diagram in Figure 10 and are described in more detail in subsections that follow. These subsections also describe the particular calibrations that were performed for the milestones, including links to archived lab notebook entries and code that was used to perform them.

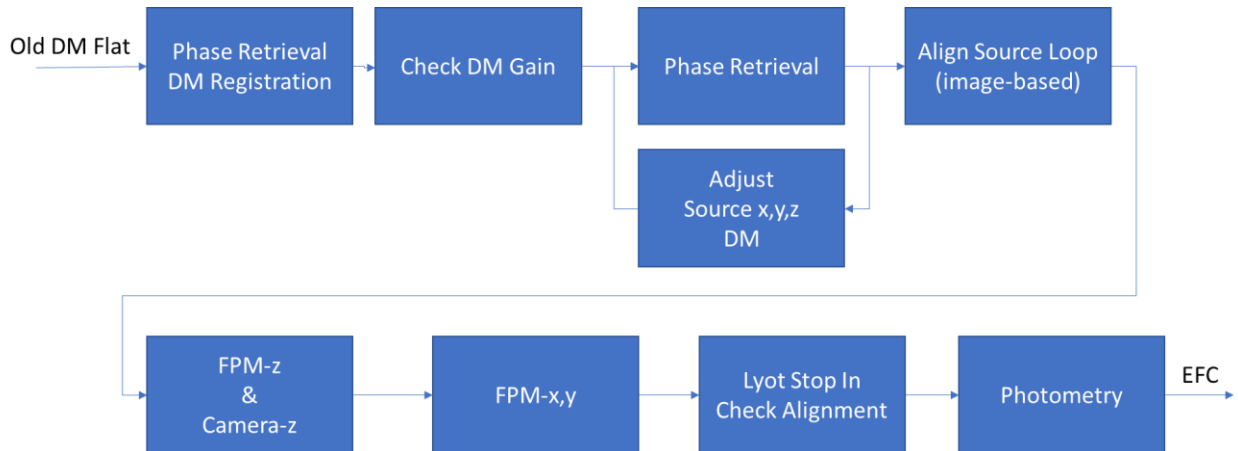


Figure 10. Calibration procedure workflow.

4.2.1 Wavefront Error and Flattening

This section describes the “Phase Retrieval DM Registration” and “Check DM Gain” blocks in Figure 10. The purpose of this procedure was to have a good starting DM setting for EFC in terms of pupil plane phase, or equivalently, a clean and symmetrical PSF in the image plane. In order to achieve this, we used a phase retrieval method (standard at HCIT) which involves taking science camera images at different locations along the z-axis and processing them using a Gerchberg-Saxton-like algorithm to obtain the phase at the pupil plane (Figure 11, first two images). Having obtained the pupil-plane phase, we performed a decomposition into the first few Zernike modes, plus a residual (remaining panels in Figure 11). Note that due to PIAA remapping, there are two sets of Zernikes: upstream of PIAA1 (conventional Zernike modes), and downstream of PIAA2 (PIAA-remapped Zernikes).

We then followed the following procedure to flatten the phase:

1. Given the current model configuration, which includes current measured testbed alignments and calibrations, initialize the model.
2. Given WFE measured by phase retrieval, use the model to determine the relative DM actuator adjustment necessary to correct the WFE, in radians.
3. Add the result from #2 to the current DM setting (used when the phase retrieval measured the WFE), apply DM gain to determine the new DM voltage array, and apply voltage limits, neighbor rules, etc.
4. Apply the new DM voltage array from #3, and record new phase retrieval.

The result after following this procedure is shown in Figure 12 and Figure 13.

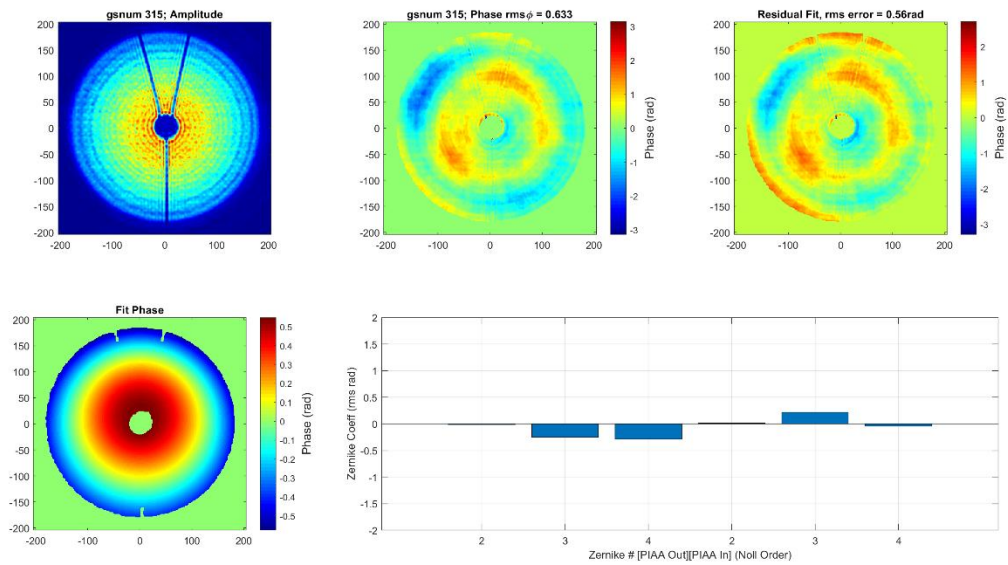


Figure 11. Top row: Pupil plane measured amplitude, phase, and residual after subtracting fitted phase consisting of tip/tilt, and defocus modes at the planes of PIAA 1 and 2 mirrors. Bottom: Fitted phase and best-fit Zernike mode coefficients.

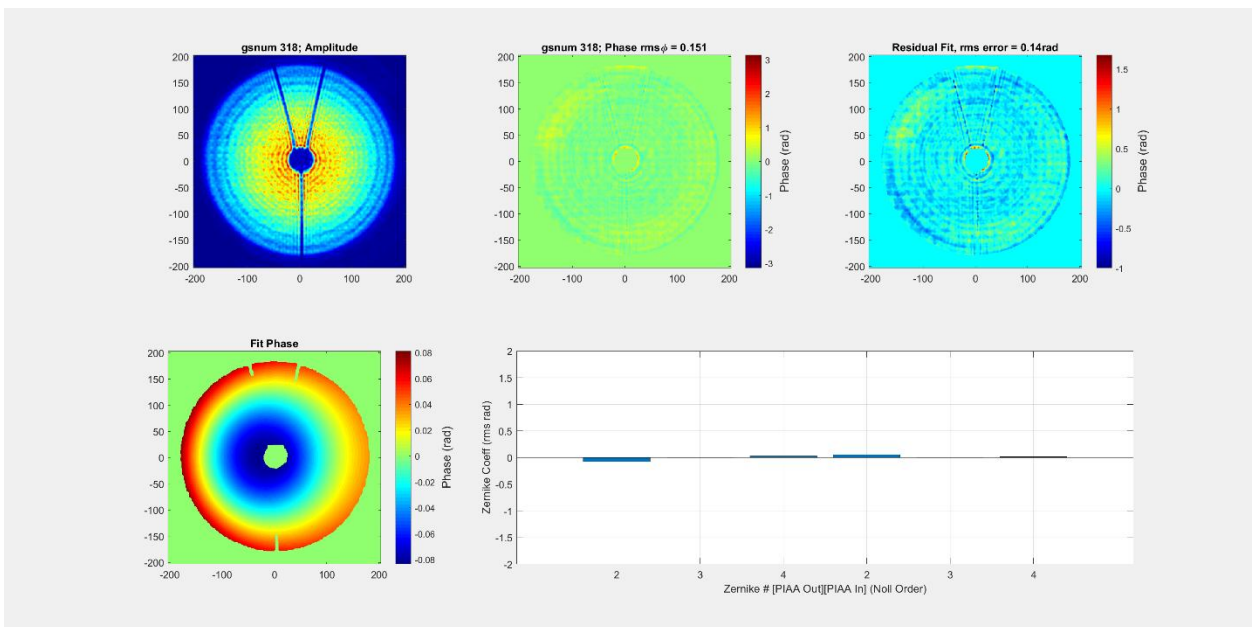


Figure 12. Top panel: Same as Figure 11, but after DM flattening. Note the flat phase in the two images in the upper right, as well as the smaller Zernike coefficients, compared to Figure 11.

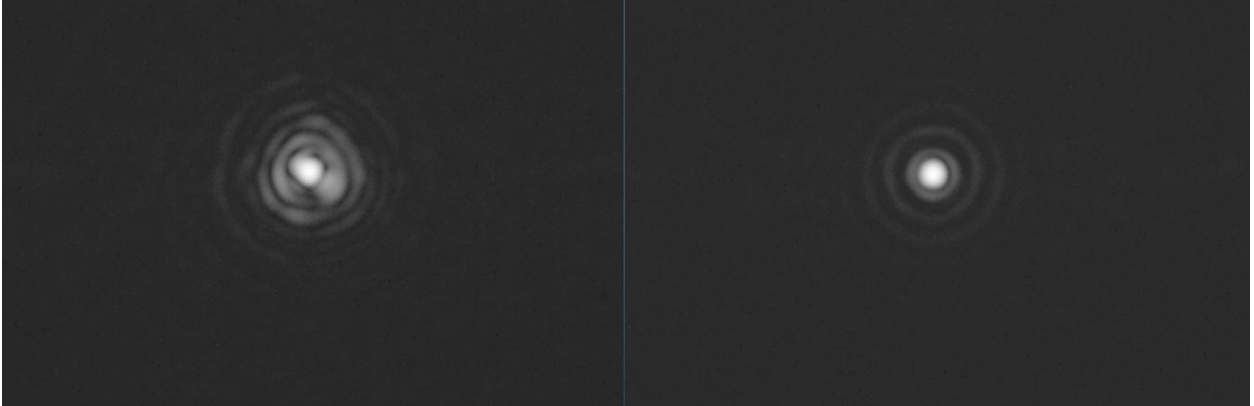


Figure 13. Science camera images of the star (point-spread functions) without coronagraphic masks, before flattening (left), and after (right).

The code used to perform this calibration for milestones 2 and 3 can be found at:
/proj/piaacmc/DM/20211007_flattening/test_flat_script.py

Lab notebook entry for this calibration can be found at: [See Source Align 2021-10-07 for source alignment to \(Web view\)](#)

4.2.2 CMC Alignment

This subsection describes the “FPM-z” alignment box in Figure 10. To align this mask, we illuminate it with diffuse light (using a diffuser), and move the mask in z until mask features are in sharp focus. Although the CMC mask is a reflective phase-only mask, some sharp phase transitions can be seen, although they are not extremely well-defined.

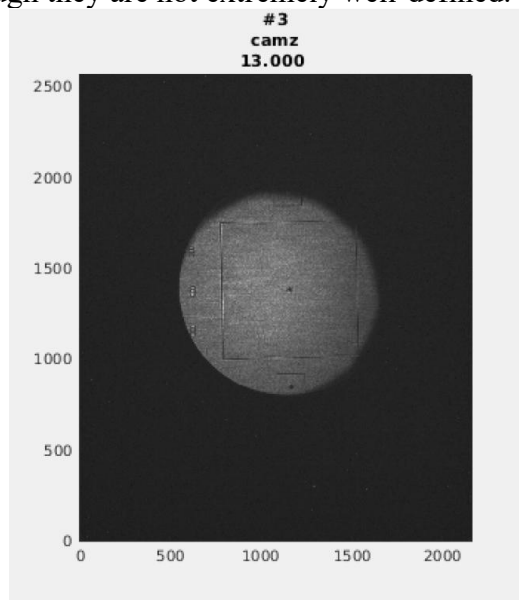


Figure 14. Image of the CMC mask illuminated with diffuse light for purposes of aligning in the z dimension (focusing the mask).

4.2.3 Lyot Mask Alignment

This subsection describes the “Lyot stop” block in Figure 10. We followed the following procedure to align the Lyot stop, which is standard practice at HCIT:

1. Take a pupil image with Lyot mask out
2. Take a pupil image with Lyot mask in
3. Register #2 to #1, and apply the registration to the Lyot mask in the EFC model.
4. Use the EFC model to generate pupil images with Lyot mask in/out and check registration

4.2.4 Source Alignment (Upstream Tip/Tilt/Focus)

This subsection describes the “align source” block in Figure 10. Tip/tilt/focus of the source upstream of the PIAA telescope creates wavefront errors distinguishable from tip/tilt/focus errors downstream of the PIAA telescope. For example, an x-translation of the source, creating an x-tilt of the wavefront upstream of the PIAA telescope, becomes a coma-like wavefront error after the PIAA telescope.

The phase retrieval procedure measures the wavefront at the back-end, that is, downstream of the PIAA telescope. Specifically, phase retrieval measures the wavefront at the camera. After translating the source in x by 2 μ m, the above wavefront error is corrected as shown in Figure 16.

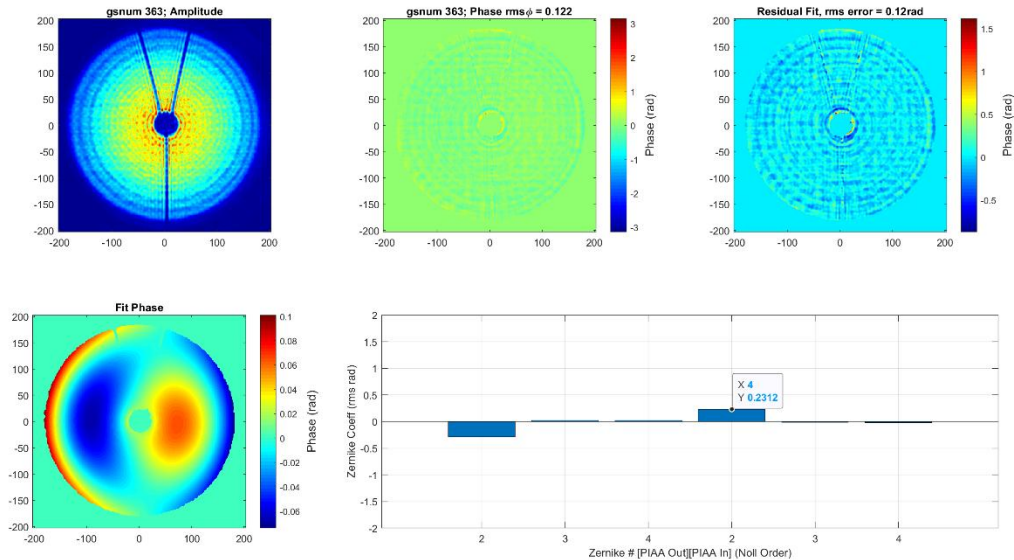


Figure 15. Phase retrieval with the fiber source misaligned in x.

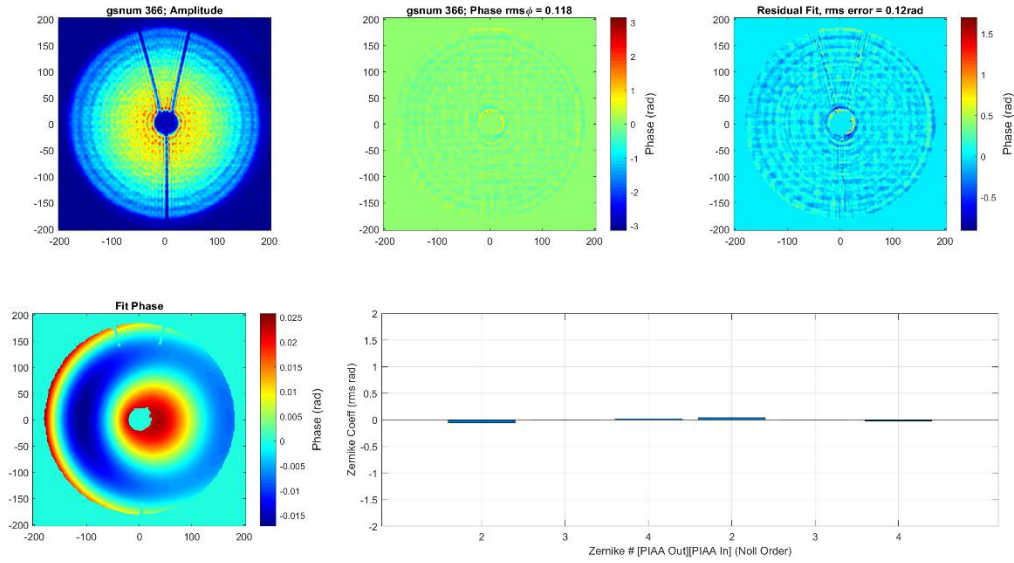


Figure 16. Phase retrieval data, with an aligned fiber source.

4.2.5 Back-end Focus

This subsection describes the “camera-z” block in Figure 10. CMC focus and camera focus (axial position of the camera) must be determined simultaneously because the CMC is reflective. Axial movement of the CMC changes the optical path length of source conjugate to the OAP. The procedure is to simultaneously conjugate the CMC mask to the camera, as imaged with the diffuser source, and check source focus on the camera, as measured with phase retrieval. Because the source alignment focus at the camera has already been established in a previous calibration step, that is the initial condition for this procedure. The sensitivity of source focus to axial movement of the CMC is twice the sensitivity of the CMC conjugate to the camera. Because the CMC is used in reflection, the apparent source conjugate moves by twice the CMC movement. For example, the graph in Figure 17 shows the camera axial position for source focus and for CMC conjugate as a function of CMC axial position. The “current position” was the initial condition for this example. The condition for simultaneous source focus and CMC conjugate to the camera is at CMC $z = -6.75\text{mm}$, and the camera at $z = 32\text{mm}$. Unfortunately, the CMC axial stage did not have range of motion to $z = -6.75\text{mm}$. Our solution was to place the CMC at $z = 0\text{mm}$, place the camera at its conjugate position to the CMC ($z = 29\text{mm}$), and used the DM to focus the source at the camera. As a result, the DM flat wavefront setting in fact include some extra defocus.

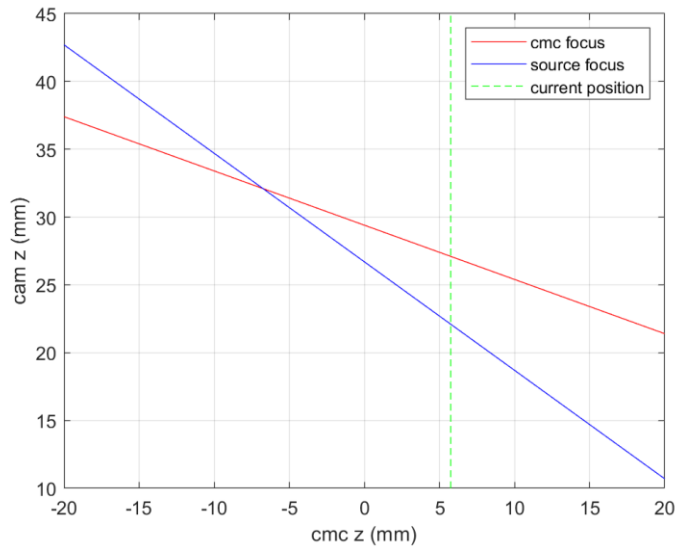


Figure 17. Cam z position at which CMC is in focus (red line) and source is in focus (blue line), as a function of CMC z position.

4.2.6 DM Registration

DM registration refers to making sure that our testbed software model has accurate locations of the DM actuators. This essentially means measuring the locations of selected actuators and adjusting the DM coordinate plane in the software model. The procedure is standard practice at HCIT and involves the following steps:

1. Record reference phase retrieval with nominal flat wavefront
2. Record a series of phase retrievals with a grid of actuators poked
3. Adjust the DM registration in the EFC model such that poking the same actuator grid in the model produces a phase map that overlays with the measure phase retrieval phase map.

4.2.7 Photometry

During the photometry calibration, we measure the number of camera counts corresponding to 10^0 contrast (i.e. the peak of the PSF with the CMC mask out). This involves iteratively measuring the brightnesses of a series of fiducial speckles that decrease in brightness by factors that are small enough to be measured with the camera (typically $\sim 10^3$). This procedure is also standard at HCIT and is described in more detail in Kern et al. 2015.

4.3 Laboratory results and milestone certification data package

4.3.1 Summary of performance against milestone metrics

We performed tests to create high contrast dark zones with EFC under several different conditions (see Figure 18), including monochromatic light with a diode laser (675nm) as well as broadband light (centered on 650nm) in a 2% and 10% band, and different sized dark zones. Figure

18 presents the dark zones after EFC converged in each case, showing the raw dark-subtracted images in the leftmost column (“unprobed”). These images consist of coherent and incoherent components shown in columns 2 and 3. (These are also referred to as “modulated” and “unmodulated”, meaning a component that is susceptible to modulation by the DM, and a component that is not.) The rightmost column shows 1D azimuthal averages of all three images. The images show light in a D-shape region that is admitted by the field stop (with some light diffracting outside the physical edges of the field stop), and the dark zone radii are shown as red circles. Typically, the dark zone is smaller than the field stop, and the EFC control region is slightly larger than the actual dark zone. Contrast values shown in the figure are averages across the dark zone.

Our monochromatic tests (first two rows in Figure 18) were done separately in the 2-4 and 4-8 λ/D regions. This was because we observed a bright speckle at the inner edge of the field stop which proved challenging to remove, and limited our contrast to 1.1×10^{-7} (4.1×10^{-8} modulated) in the 2-4 region. The nature of this speckle remains unclear, and in particular whether or not it has to do with coronagraph hardware or testbed itself. This speckle was originally thought to be due to testbed jitter and tip/tilt sensitivity, but this has been ruled out (see section 4.5). Another possibility is diffraction from the field stop edge. The field stop is not a fundamentally required component of a coronagraph and is present to prevent practical issues such as camera blooming and other pixel cross-talk. (In which case a camera with less blooming and cross-talk would mitigate this.)

Contrast in the 4-8 region was much deeper, at 9×10^{-9} raw (1.6×10^{-9} modulated), proving that PIAACMC components impose no incoherent light limits down to at least 1.6×10^{-9} levels. The unmodulated light is at 7.4×10^{-9} levels and is what is ultimately limiting our performance. It is not yet known whether this light is due to PIAACMC components or auxiliary testbed hardware and environment. However, this unmodulated light was originally much higher, which was traced to several effects external to the PIAACMC coronagraph, such as ghosts and scattered light, and this may still be what’s limiting both the raw and modulated contrast.

Performance in the 2% band is only marginally worse than the monochromatic light 4-8 λ/D case, and may in fact represent better performance considering that wavefront control was applied over a larger dark zone (3.5-8 λ/D). We conclude that our system is insensitive to increasing the band to 2%, and that we do not have ghosts whose optical path difference is between the coherence length of the monochromatic diode and 2% band source.

Finally, raw contrast performance in a 10% band is 1.9×10^{-8} in 10% between 3.5-8 λ/D , which is comparable (within roughly a factor of 2) of monochromatic and 2% cases. Furthermore, levels of unmodulated light are similar. The greatest difference is the modulated light, which at 9.4×10^{-9} is almost an order of magnitude greater than the narrowband case. Analysis of different wavelengths in the 10% band reveals a quadratic dependence of contrast vs. wavelength, with the contrast at the central wavelength being much closer to the narrowband case. Therefore, unlike the monochromatic case, broadband contrast appears to be limited by the chromaticity in our system, rather than incoherent light. However, according to simulations of broadband EFC, this chromaticity should be suppressible, and it may be the case that we have simply not spent enough time on tuning our broadband models (we focused on monochromatic and narrowband tests as a prerequisite for broadband).

In what follows, we describe the milestone certification data package (actual data files are available separately).

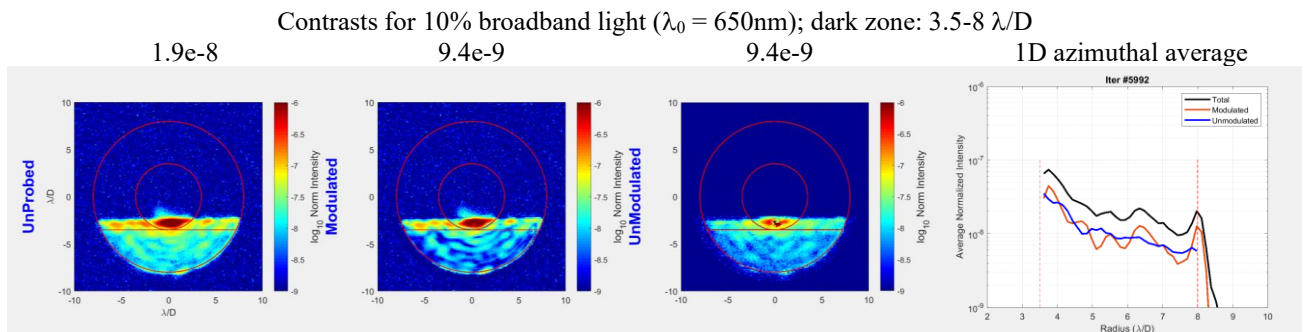
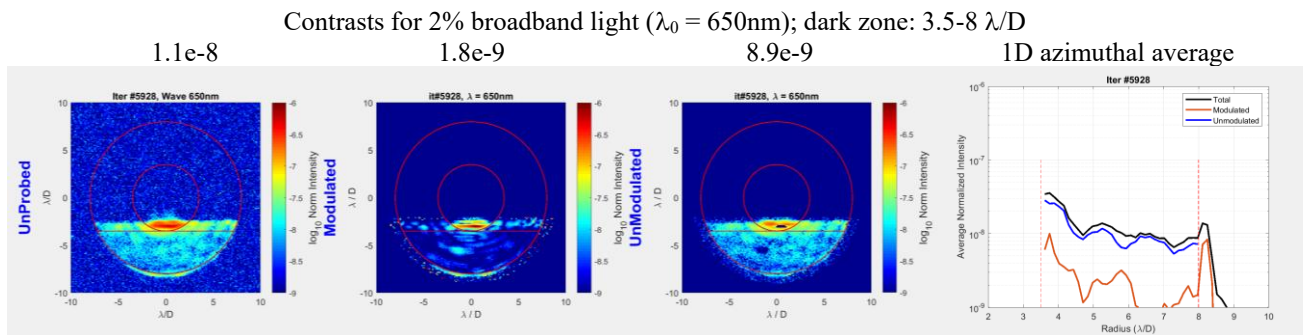
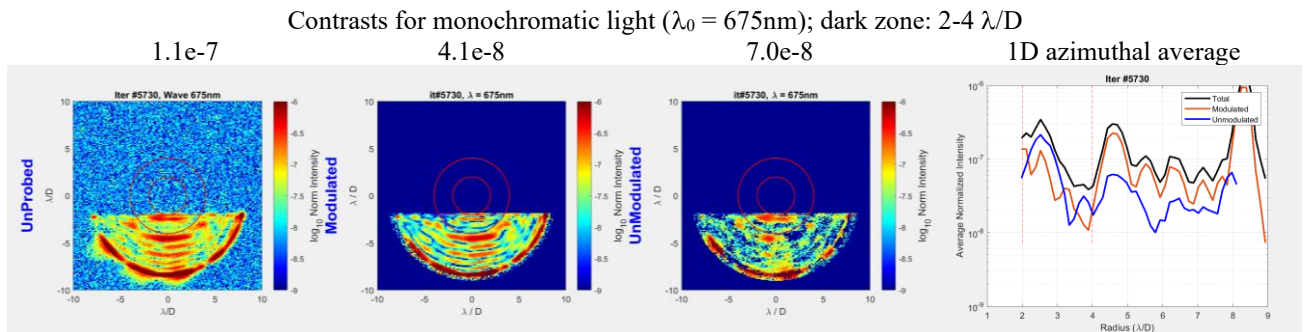
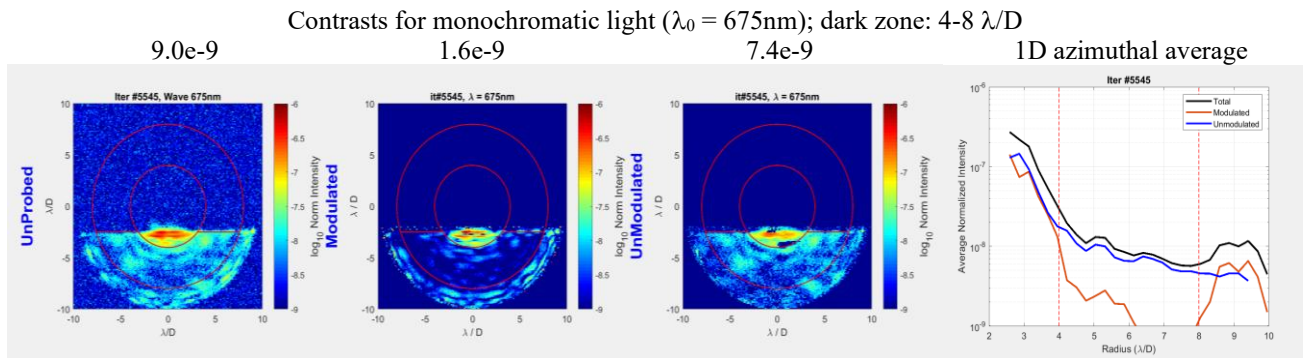


Figure 18. Laboratory results. Rows correspond to different wavelength bands and dark zones (indicated by red outlines). Columns represent, respectively, raw (unprobed), coherent (modulated), and incoherent (unmodulated) images, and 1D azimuthal averages. A D-shaped field stop was used to prevent blooming of surrounding bright speckles.

4.3.2 Calibrated Images of the coronagraph transmittance profile (item #2 in certification data package)

The measured transmittance profile of our coronagraph is shown in Figure 19 (without field stop) and Figure 20 (with field stop). These plots were obtained by moving the star source by small amounts spanning $\pm 10 \lambda/D$ on-sky in x (horizontal) and 0-10 λ/D in y (vertical) with respect to the camera images in Figure 18. The x-axis shows the source displacement, and the y-axis shows total energy measured in the dark hole, and normalized to maximum transmittance. Both measurements were taken with the DM set to a high contrast dark hole setting. To measure the sensitivity of transmittance to DM setting, we also measured the y-transmittance with a flat DM, which is overlaid on the left plot in Figure 19 with a dashed red line. As can be seen, the DM settings we used to create a dark hole are not strong enough to appreciably affect the coronagraph transmittance curves.

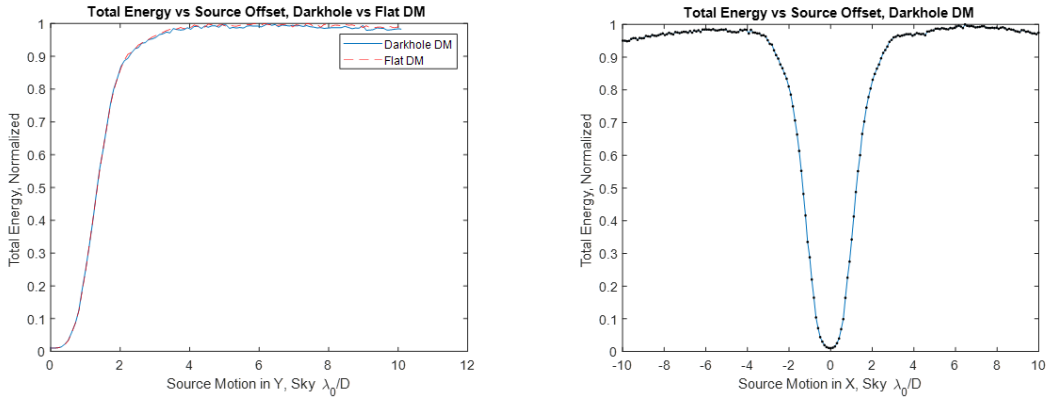


Figure 19. Measurements of the coronagraph energy transmittance vs. off-axis point source (without field stop). Left: source motion in y direction (vertical). Right: source motion in x-direction (horizontal)

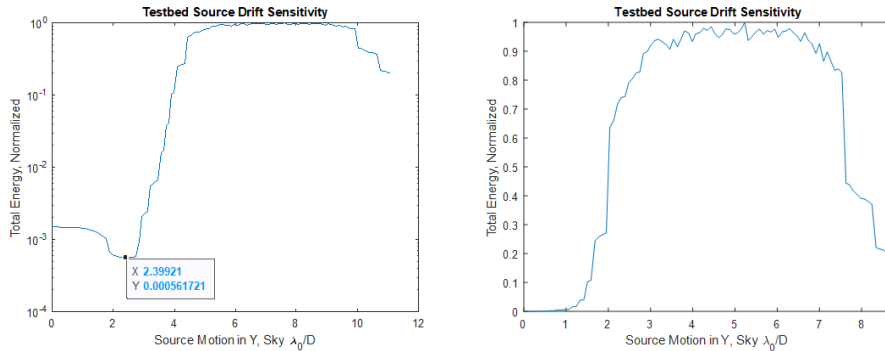


Figure 20. Measurements of coronagraph transmittance vs. off-axis point source (with field stop)

The inner working angle measured from Figure 19 (without field stop) is $1.55 \lambda/D$, using empirically-measured PIAA magnification, and represents the IWA limited by the PIAA mirror and focal plane masks. However, the inner edge of our field stop further limits the IWA. This is shown in Figure 20, which shows the transmittance with the field stop in place. The measured IWA from these curves is $1.9 \lambda/D$.

4.3.3 Calibrated Images & Residual Light in the Dark Zone (items #3-5 in the certification data package)

This section describes the calibrated images and the data set, as well as histograms of brightness distribution of pixels in the high contrast dark field. We start with a summary of our results in table form below. Each row corresponds to one of our four tests with different wavelengths, bands, or dark zone regions (LD = laser diode). Columns show the band, dark zone, and different representations of normalized intensity: mean of total light image, mean of coherent image, mean of incoherent, standard deviation of coherent image, and normalized standard deviation.

Band	Dark Zone	\bar{m}	\bar{m}_{coh}	\bar{m}_{inc}	σ_{coh}^2	$\sigma_{coh}^2/\bar{m}_{coh}$
675nm LD	4 to 8 λ/D	9.0e-9	1.6e-9	7.4e-9	1.1e-9	0.69
675nm LD	2 to 4 λ/D	1.1e-7	4.1e-8	7.0e-8	5.5e-9	0.13
650nm 2%	3.5 to 8 λ/D	1.1e-8	1.8e-9	8.9e-9	1.3e-9	0.72
650nm 10%	3.5 to 8 λ/D	1.9e-8	9.4e-9	9.4e-9	3.1e-9	0.33

4.3.3.1 Narrow Band, 4 – 8 λ/D

The best contrast for the narrow band case, with the dark zone between 4 and 8 λ/D occurred during a run when EFC correction was continuing to search for better contrast, but the dark contrast was dominated by unmodulated light. At the best contrast, there were about 40 iterations where modulated speckles were measured with good discrimination, but the EFC correction introduced as much new modulated light as removed with each iteration. Figure 21 shows total, unmodulated, and modulated mean normalized intensity over the dark zone for the series of iterations where best contrast was achieved.

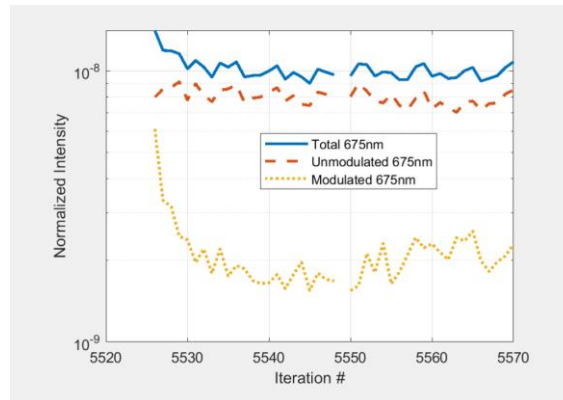


Figure 21. Mean total, unmodulated, and modulated contrast for several iterations at best contrast, narrow band, 4 to 8 λ/D . Best contrast was achieved at iteration 5545 (Figure 22).

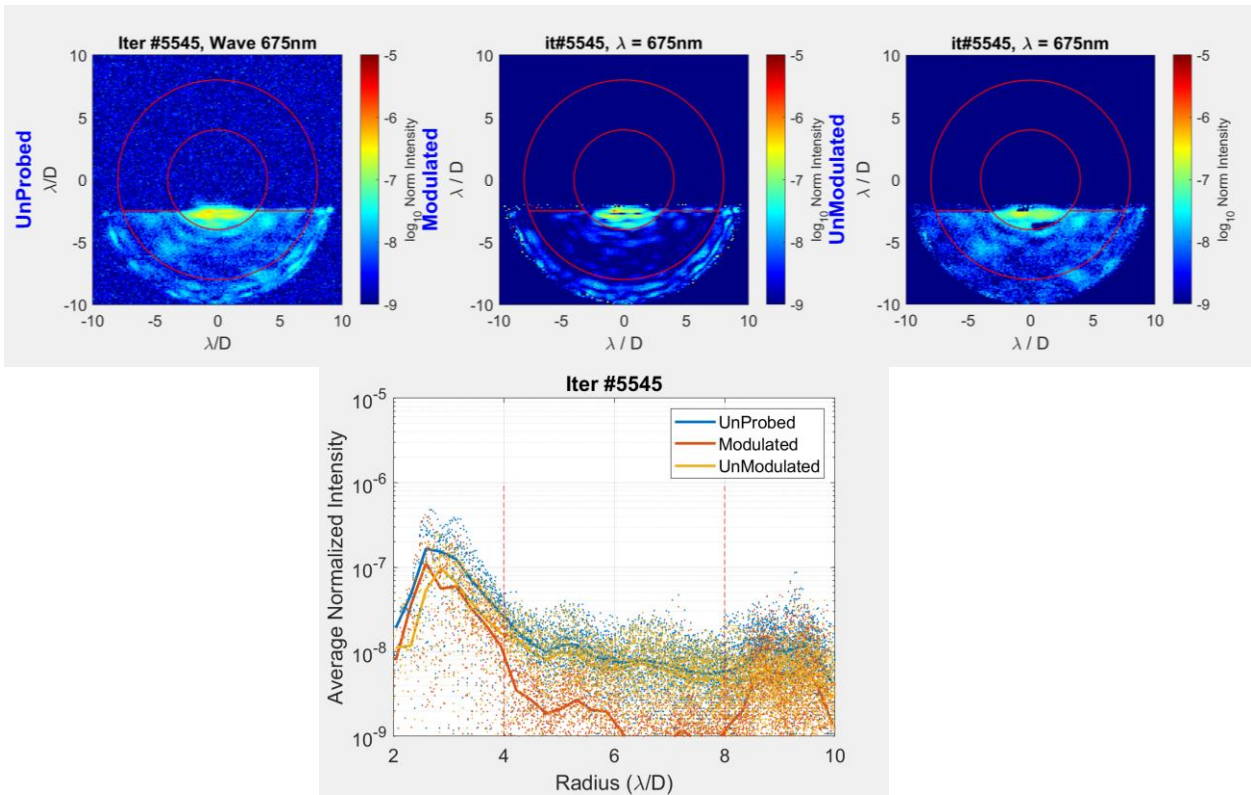


Figure 22. Dark zone images at best contrast; b. radial scatter plot of normalized intensity across the dark zone.

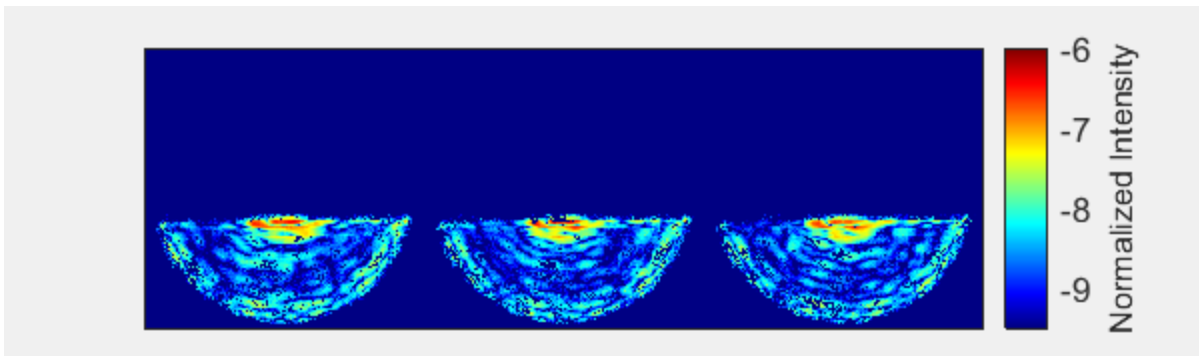


Figure 23. Example sequence of modulated intensity for three iterations. The speckle morphology is different for each iteration.

By definition, the modulated component of the measured intensity in the dark zone is that part that can be affected by the DM. With each iteration, the DM is modulated to probe the E-field in the dark zone. With an estimate of the E-field, the electric field conjugation (EFC) optimization determines a new DM setting that is estimated to cancel the estimated E-field. Evidently, in the series of iterations shown here, the E-field is altered with each iteration, but its average intensity is not reduced. There are several possible causes for this lack of progress. For example, model error resulting from testbed calibration error can cause errors in the Jacobian used in EFC. Another example is nonlinearity in the probe estimation causes errors in the estimated E-field. It is possible that the regularization used in the EFC optimization reduces the degrees of freedom to the extent that there is no solution in the available solution space. Finally, since the modulated component is approximately one-fifth the intensity of the unmodulated light, and noise, such as shot noise, in

the unmodulated light is falsely interpreted as modulated light, biasing the estimate of the modulated E-field.

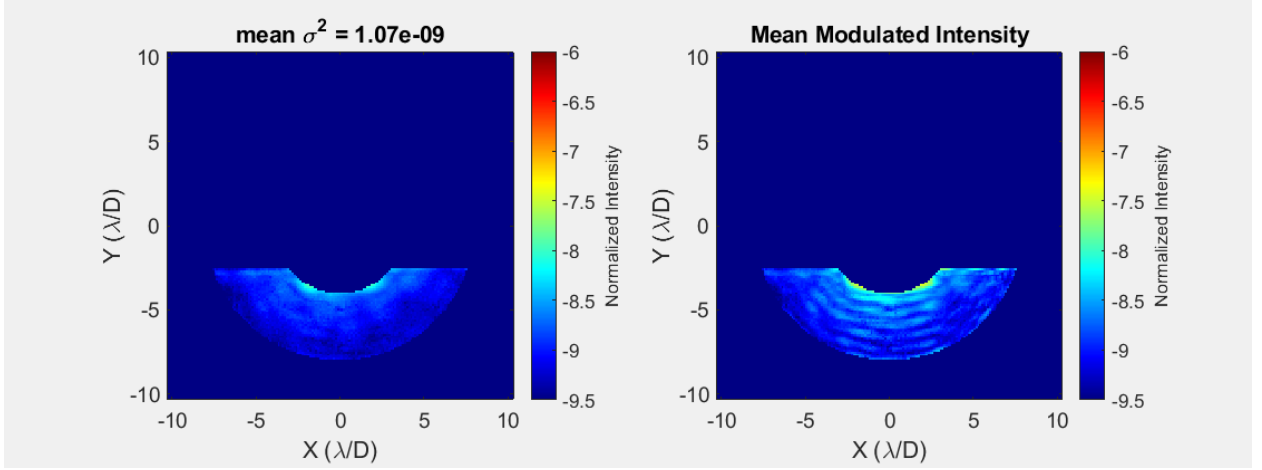


Figure 24. pixel-by-pixel variance and mean of the modulated intensity across the dark zone. The sample size for estimating the variance is 40 iterations.

To understand the contribution of the dynamic part of the estimated modulated E-field compared to the static contribution, we look at a few simplistic measures. We define the dynamic contribution as that part of the modulated E-field that changes from iteration to iteration. The pixel-by-pixel variance across the 40 iterations estimates the dynamic contribution (Figure 24). The dynamic portion of the total modulated intensity is about two-thirds.

Now that we have determined that the dynamic speckle “boiling” is the major contributor to the modulated light, it is instructive to ask if the changing E-field for each iteration is correlated. We calculate a correlation matrix,

$$R(i, j) = \frac{\sum_{pixels} E_i^* E_j}{\sqrt{\sum_{pixels} |E_i|^2 \sum_{pixels} |E_j|^2}}.$$

Figure 25a displays $|R(i, j)|$. Similarly, a covariance matrix of the covariance of the E-field between iterations indicates the normalized intensity attributable to a common E-field. Figure 25b displays,

$$\text{Cov}(i, j) = \sum_{pixels} (E_i - \mu_i)^* (E_j - \mu_j) / (N_{pixels} - 1).$$

If EFC nulling of the modulated E-field had converged to a minimum in the usual manner, then the modulated E-field would be relatively constant from one iteration to the next, and the correlation matrix and covariant matrix shown in Figure 25 would be nearly uniform. However, for this run, the EFC converged to a “boiling” state, and the covariance matrix indicates that much of the intensity in each iteration is of a different morphology from that of the other iterations. Furthermore, there is little indication of an oscillating of the estimated E-field, which might be expected if, for example, EFC were mostly moving in the right direction overstepping with loop gain.

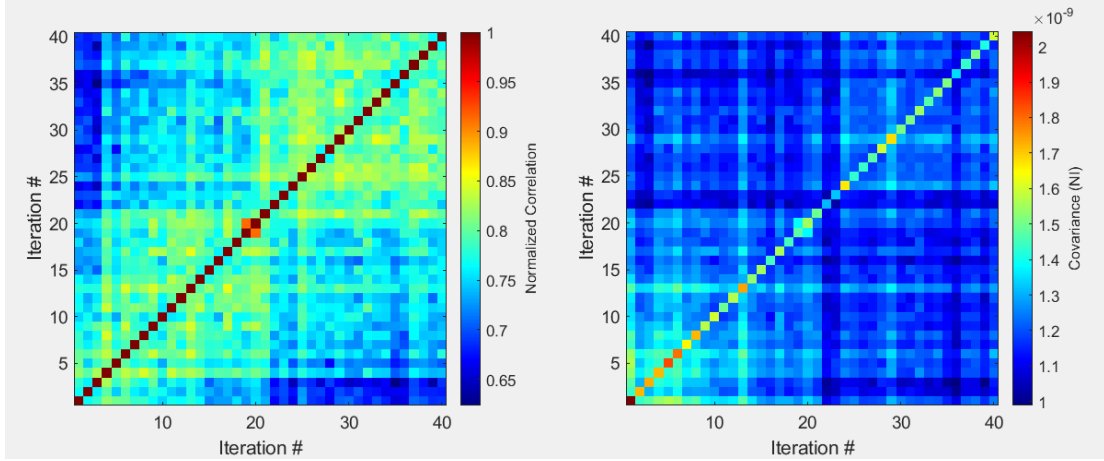


Figure 25. a) Correlation matrix of estimated E-field by iteration; b) covariance matrix of estimated E-field by iteration, indicating the modulated intensity that is common to each iteration.

4.3.3.2 Narrow Band, $2 - 4 \lambda/D$

In contrast to the EFC result above for working angle greater than $4 \lambda/D$, the dark zone at near working angles converged to a steady state – see results in Figure 26. Comparing the variance of the modulated component to the mean modulated intensity (Figure 27), we see that the variance is small and shot noise limited. Furthermore, the modulated speckles constitute a greater portion of the total intensity in the dark zone than it did for the wide angle result. Because of the stability of the modulated speckles, the limits of EFC to find a better solution are likely not due to model mismatch, but rather the available degrees of freedom or a local minimum. Along this line of reasoning, the reason this EFC result is worse than predicted by design might be due to the differences between the real testbed and the original design.

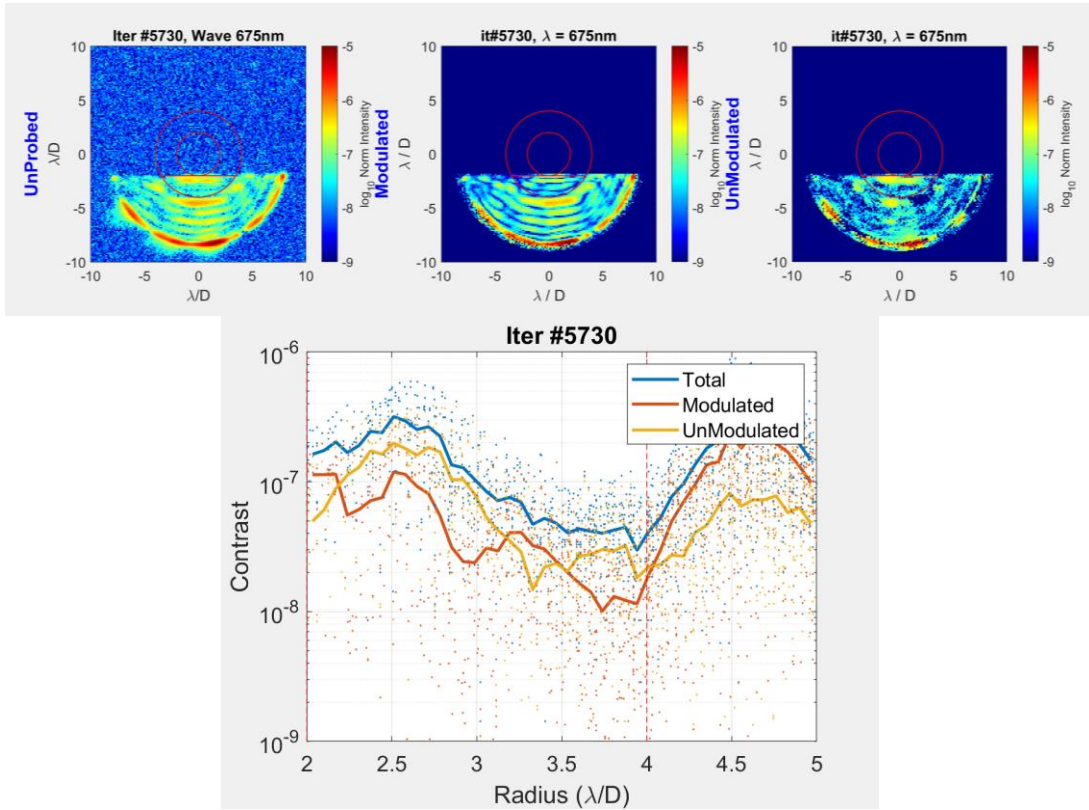


Figure 26. Contrast results for narrowband, 2-4 λ/D case.

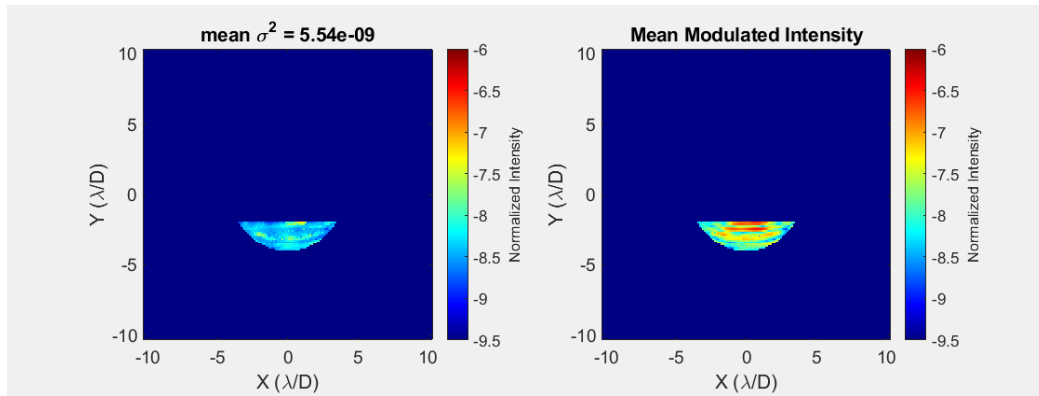


Figure 27. Mean modulated intensity and mean pixel-by-pixel variance of the dark zone for 2 – 4 λ/D , averaged over 30 iterations after EFC convergence.

4.3.3.3 650nm, 2% BW, 3.5 – 8 λ/D

Replacing the laser diode of the above two EFC results with the NKT supercontinuum laser, we first run EFC with a narrow 2% bandwidth and have similar results to EFC with the laser diode. This result is not exactly a controlled comparison to the first laser diode EFC result because here the dark zone is 3.5 – 8 λ/D , whereas it was 4 – 8 λ/D for the first laser diode result. However, the result is very similar, limited by unmodulated light and the “boiling” modulated speckles.

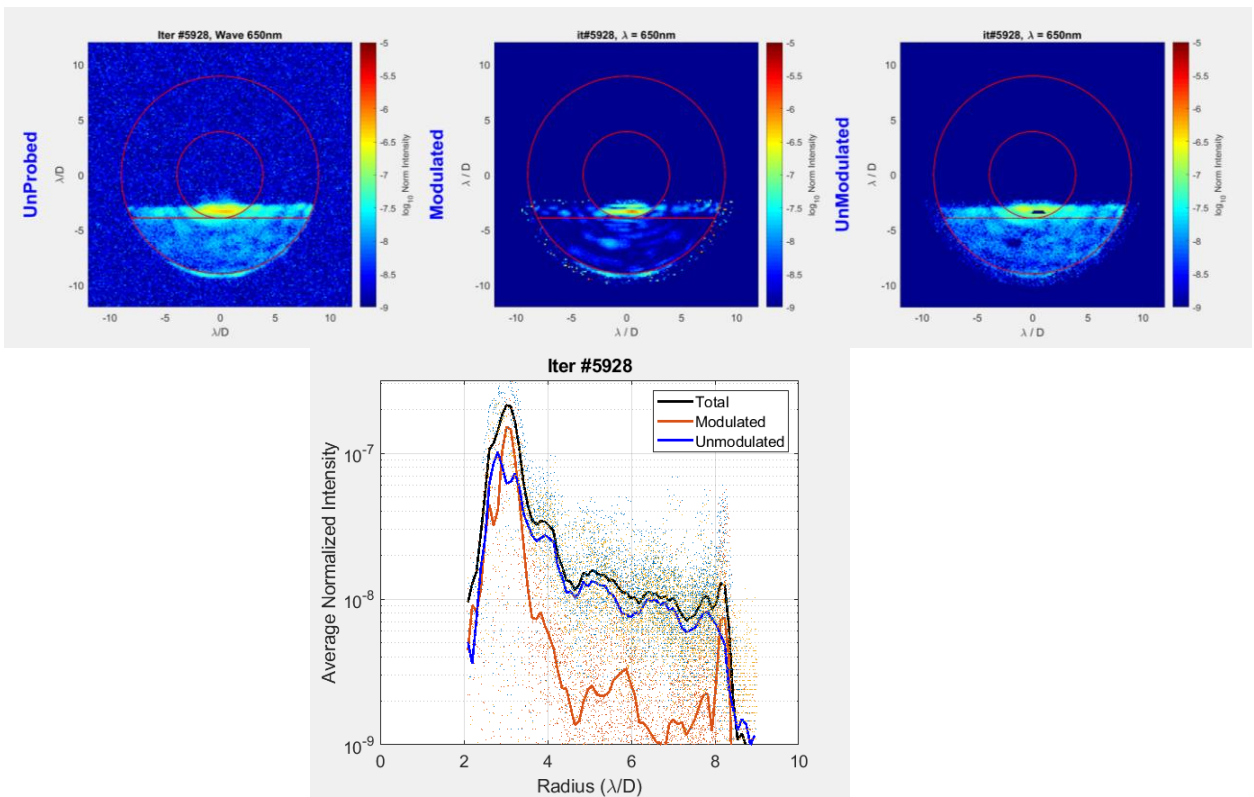


Figure 28. Results for 2% band, 3.5-8 λ/D case.

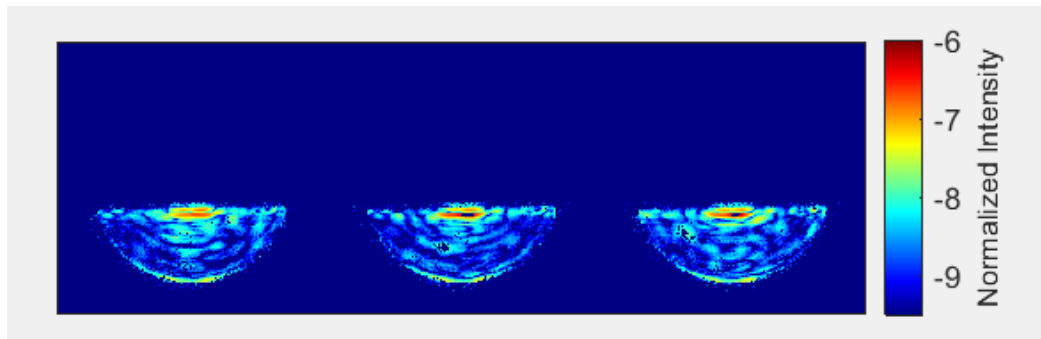


Figure 29. Modulated Intensity for three successive iterations near the best dark zone. The modulated speckles have different morphology for each iteration.

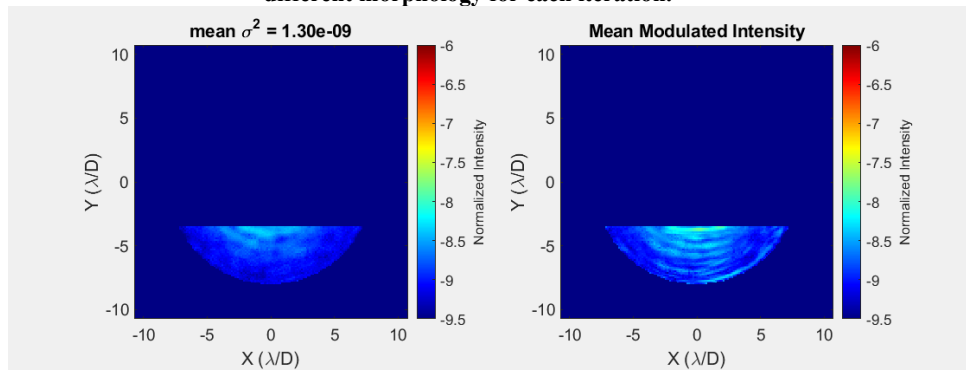


Figure 30. Mean modulated intensity and mean pixel-by-pixel variance of the dark zone for 3.5 – 8 λ/D , averaged over 30 iterations after EFC convergence.

4.3.3.4 650nm 10% BW, 3.5 – 8 λ/D

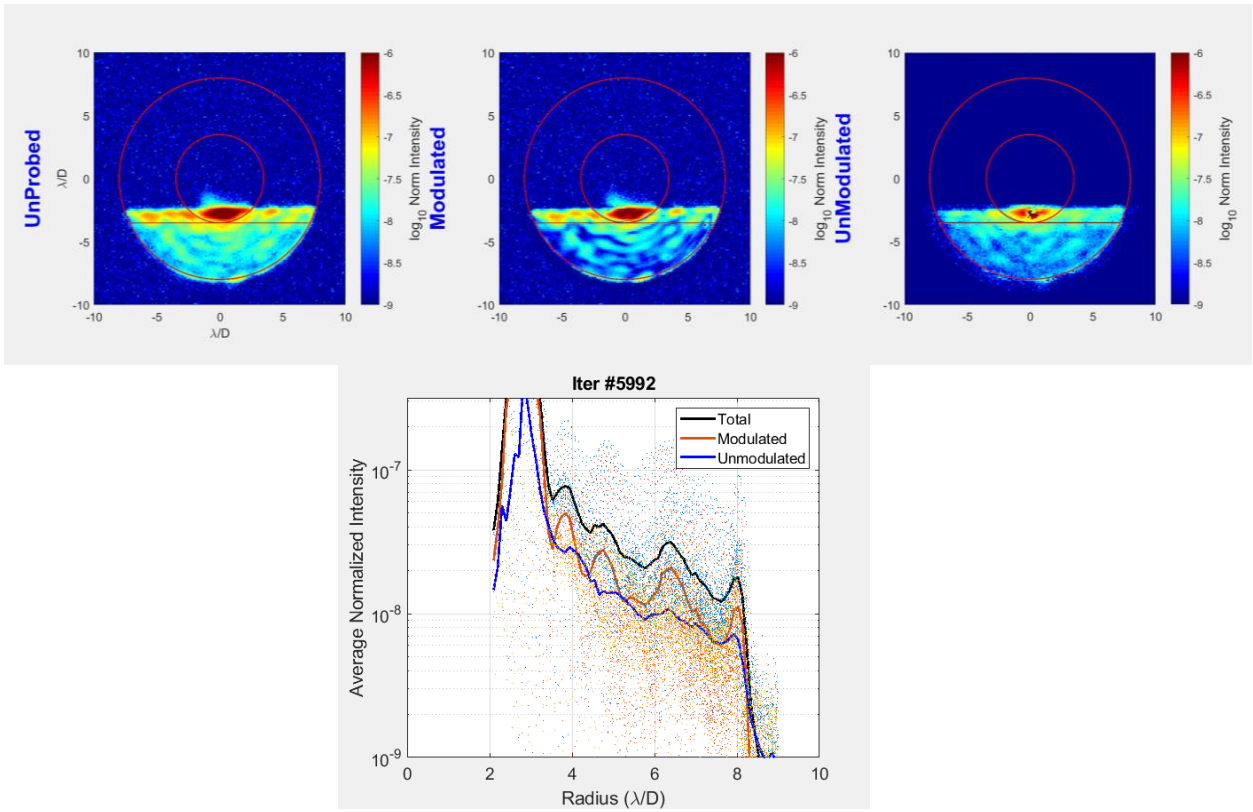


Figure 31. Results for 650nm, 10%, 3.5-8 I/D case

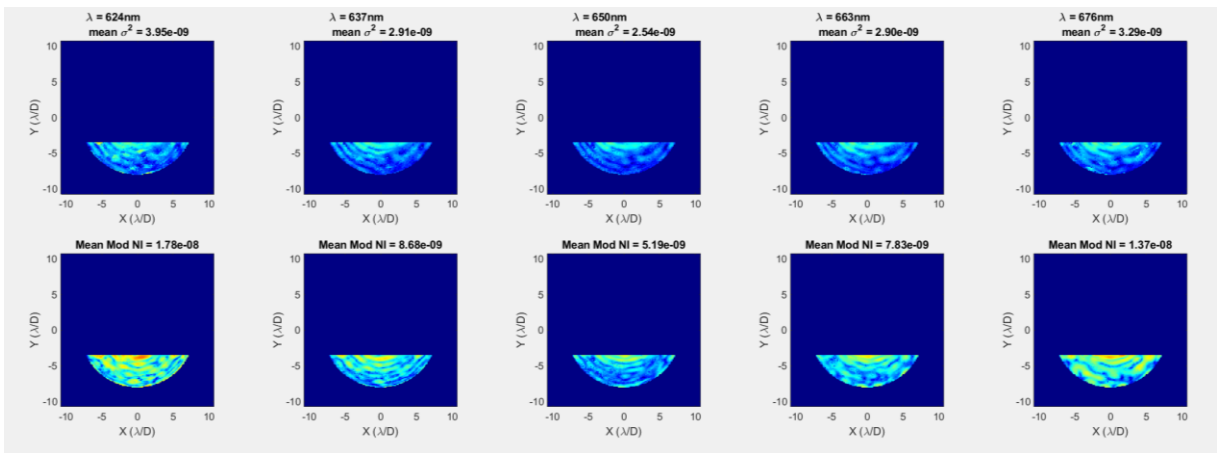


Figure 32. Variance of the E-field and mean normalized intensity for each 2% subband.

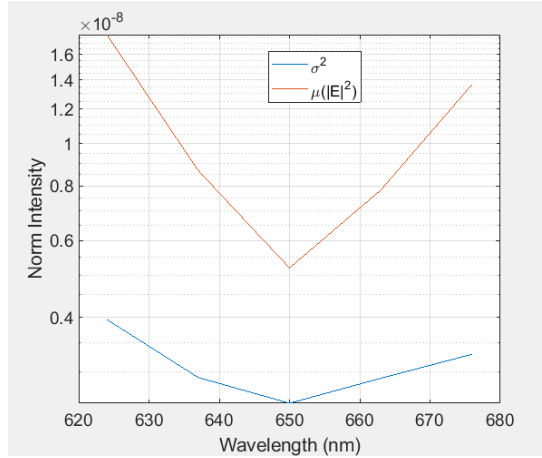


Figure 33. The variance of the modulated intensity is not as strongly dependent on wavelength as the mean modulated intensity, averaged over the dark zone.

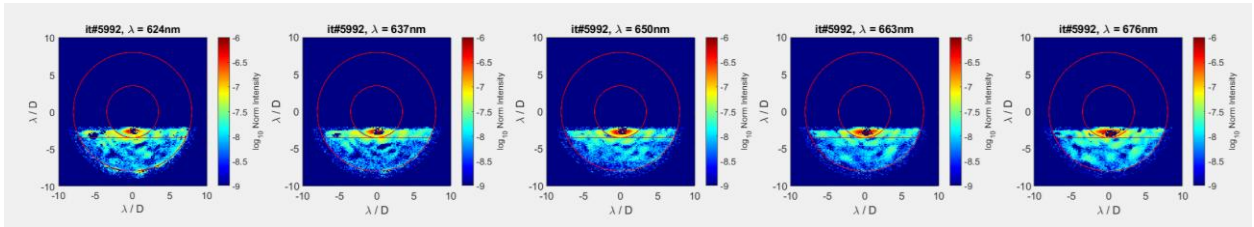


Figure 34. Unmodulated normalized intensity for each wavelength.

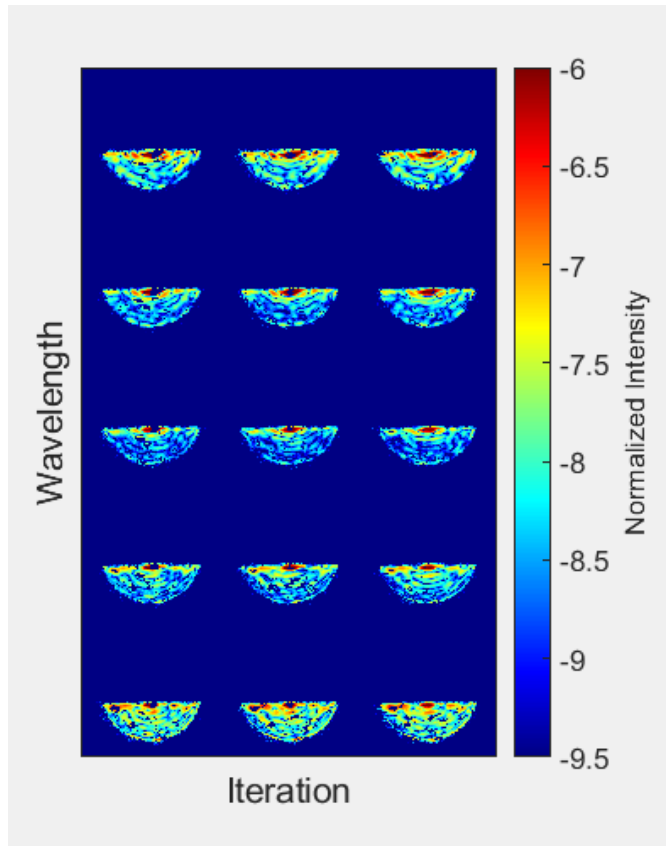


Figure 35. Dark zone variations with wavelengths and iterations.

4.3.4 Drift

This section shows the results of our stability measurements of normalized intensity of the 650nm, 10%, 3.5-8 λ/D case. The testbed was stable for about 1 hour, 20 minutes before mean modulated intensity started to degrade from the nominal of $2e-9$.

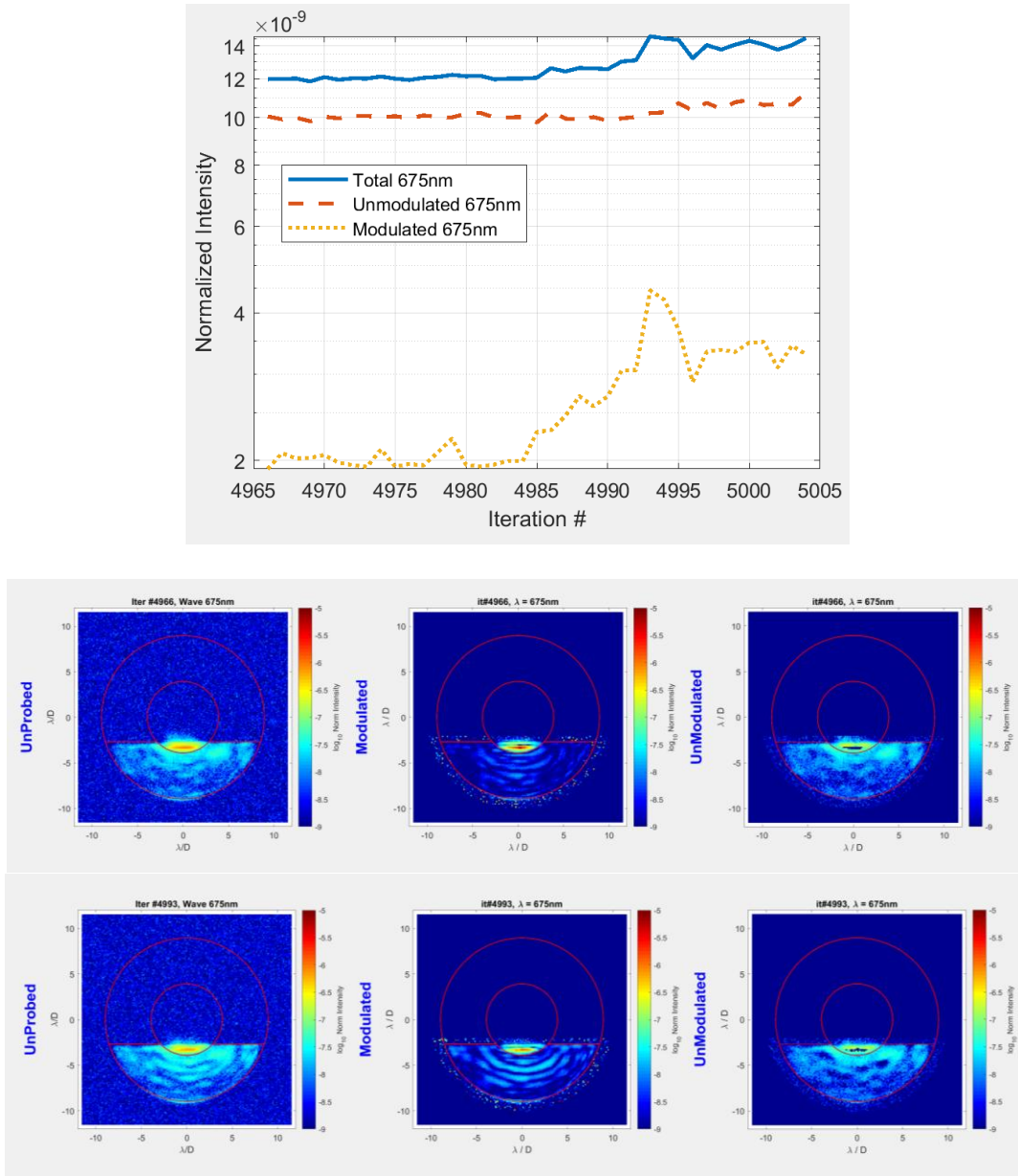


Figure 36. Normalized intensity stability in the dark zone. Top: normalized intensity vs. iteration. Middle: Iteration 4966, beginning of drift test. Bottom: iteration 4993, end of drift test. As before, columns represent, respectively, raw (unprobed), coherent (modulated), and incoherent (unmodulated) images.

4.4 Tip-tilt sensitivity measurements

One of the historical weaknesses of PIAA family of coronagraphs is its sensitivity to tip/tilt aberrations (and by extension, to stellar angular size). Our LUVOIR A was designed with improved tolerance to tip/tilt aberrations and according to models is insensitive to $\sim 0.02 \lambda/D$ diameter stars down to $\sim 1e-9$ contrast. However, does actual tolerance match the design?

To test this, we moved our source off axis by small amounts and collected the resulting coronagraphic off-axis PSFs. Raw contrast measurements both in the model and testbed are shown in Figure 41, for the full 2-8 λ/D dark zone. On this figure, solid thin lines show the model, and dashed lines show the measurement. The “x” and “y” coordinates correspond to the orientation shown in the intensity figures throughout this document (e.g. Figure 39 -- in other words, “x” corresponds to motion of the source parallel to the straight edge of the dark zone, and “y” is perpendicular – as might be expected, sensitivity is greater in “y” than in “x”). However, all of these curves mix modes that are insensitive to tip/tilt (due to the underlying speckle field), and terms that are sensitive to tip/tilt (which is what we really want to compare). The former is responsible for the horizontal parts of the curves, which are greater for the empirical case due to the contrast limitations described in section 3. This mixing of modes makes the comparison non-trivial if the underlying speckle fields are significantly different between empirical measurements and model, as they are in Figure 41. However, it is possible to disentangle the pure tip/tilt terms. The details of how this is done is beyond the scope of this paper (and will be covered in a journal paper), but our empirical estimates of pure tip/tilt terms are shown as solid lines, which compare well to the slanted portions of the design curves where the tip/tilt terms dominate. We conclude that the observed sensitivity to tip/tilt aberrations compares well to the designed one.

4.4.1 Tip-Tilt Sensitivity

One indicator of coronagraph performance is its sensitivity to jitter at expected testbed levels. Here, we provide a comparison between the jitter sensitivity of the coronagraph design, with that expected from the testbed model, and the empirically measured sensitivity from testbed measurements. We first measure the testbed jitter levels by high-frequency measurements of the unocculted PSF. We then measure the coronagraph sensitivity by performing a quadratic fit across the dark zone as a function of source displacement. We compare the estimated contrast levels due the measured testbed jitter level and the coronagraph sensitivity in all three cases. This method of estimating the contrast at the expected jitter levels in the testbed has the advantage of not being limited by the achieved contrast floor in the testbed which may be caused by a different limiting factor.

Empirical Jitter Level

We use the high-burst mode on the science camera without the CMC mask in place to measure the level of testbed jitter. We recorded the unocculted PSF centroid across 4000 frames taken at a cadence of ~ 1000 frames per second in five separate trials. An example trial measuring the PSF centroid is shown in Fig. 37 to the right. Across the different trials we have the empirical jitter level across each axis as $\sigma_x = 9.7e-3 \lambda/D$ and $\sigma_y = 3.4e-3$. We can estimate the expected contrast level from the testbed jitter across each axis as:

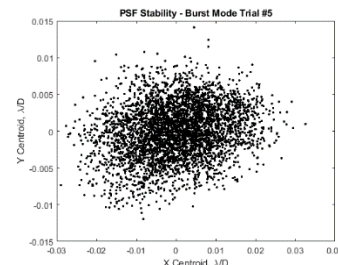


Figure 37 Empirical jitter level measurement by recording centroids PSF centroids.

$$I = \left| \frac{dE}{dx} \right|^2 \sigma_x^2 + 2 \left| \frac{dE}{dy} \right|^2 \sigma_y^2$$

4.4.2 Coronagraph Jitter Sensitivity

The jitter sensitivity is obtained from fitting a quadratic coefficient from data taken across the dark zone by displacement of the source described the following equation:

$$\frac{d^2 I}{dx^2} = 2 \left| \frac{dE}{dx} \right|^2 + 2 \operatorname{Re} \left\{ \frac{d^2 E}{dx^2} E^* \right\}$$

Where I is in the intensity at each pixel in the dark zone measured at a set of different source displacements x (or y depending on the displacement axis), and E is the corresponding electric field in the dark zone. The coronagraph's jitter sensitivity term is $\left| \frac{dE}{dx} \right|^2$ but this cannot be directly measured. Instead, the coronagraph's jitter sensitivity must be approximated from quadratic coefficient fit from the pixel-wise displacement data across the dark zone $\frac{d^2 I}{dx^2}$. In general, the intensity includes a

mixing term with underlying electric field speckles which in cases of poor contrast can be significant. These terms can be individually computed for the model, but for the testbed only intensity measurements are possible so the empirical testbed sensitivity will be measured

assuming the mixing term is negligible so that $\frac{d^2 I}{dx^2} \approx 2 \left| \frac{dE}{dx} \right|^2$. The quadratic coefficient fit for a sample pixel measurement is shown in Fig. 38 above. Performing this measurement pixel-by-pixel generates a 2D jitter sensitivity across the dark zone. In Fig. 39 below, we measure the expected contrast due to each term of the jitter sensitivity equation above from the testbed control model. The fitted quadratic coefficient term across the dark zone is shown on the left, the numerical jitter sensitivity term is shown in the center, and the mixing "D2 term" is shown on the right which is estimated to be nearly an order of magnitude smaller than the jitter sensitivity term. This shows that the quadratic coefficient fit is a good representation of the jitter sensitivity to within 10% as predicted by the model.

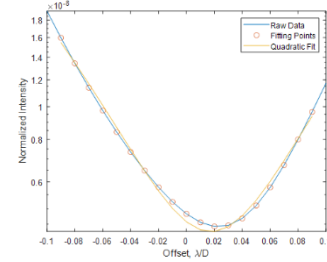


Figure 38 Sample pixel-wise measurement of jitter sensitivity by fitting the quadratic coefficient intensity measurements as a function of source displacement

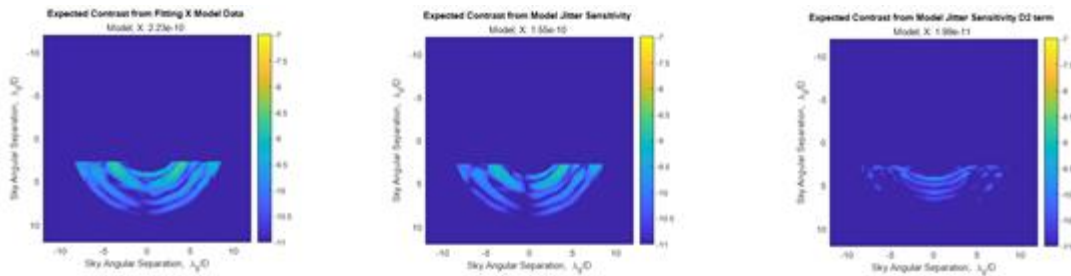


Figure 39 Expected contrast for testbed model due to: (Left) fitting quadratic coefficient to intensity as a function of source displacement, (Center) numerical jitter sensitivity, (Right) mixing of jitter sensitivity with underlying speckles.

We next compute the expected level due to the jitter sensitivity and testbed jitter levels from the quadratic fit for each of the two displacement axes and their total for the original design, the testbed control model, and from testbed measurements below:

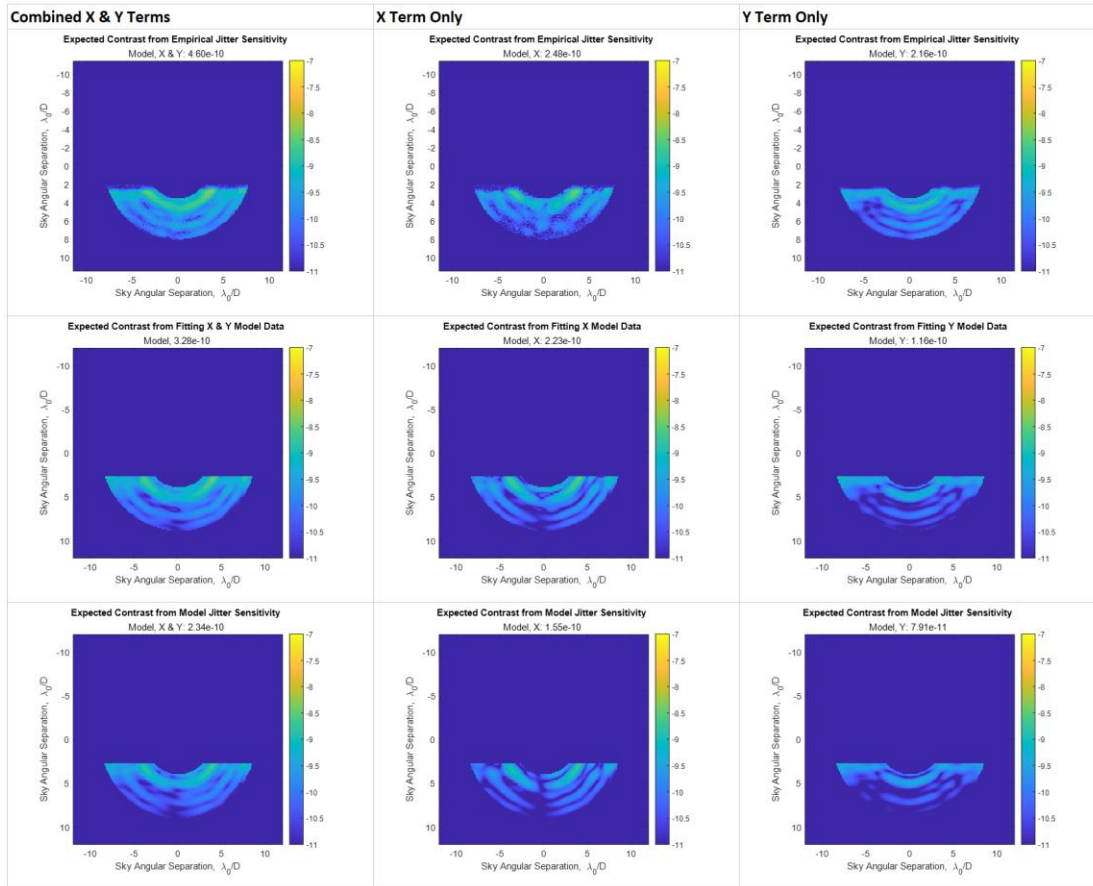


Figure 40: Expected contrast due to the quadratic fitted coefficient for the combined measured jitter level (left column), the x-axis only (center column), and the y-axis only (right column). These are computed from empirical testbed data (top row), the testbed control model (center row), and from the original design (bottom).

These show the expected contrast level from the empirical jitter sensitivity is within a factor of 2x from the original design, and a factor of 1.4x from the testbed wavefront control model. In addition the morphology of the jitter sensitivity shows good agreement across all cases. As a note, we do expect a greater level of jitter sensitivity along the y-axis due to the non-azimuthally symmetric nature of the D-shaped dark zone. Finally, we show the mean raw empirical intensities measured in the testbed’s dark zone as a function of source displacement and compare

this with the design intensities in the dark zone. Also shown is the estimated contrast level from the measured PIAACMC jitter sensitivity as a function of jitter levels:

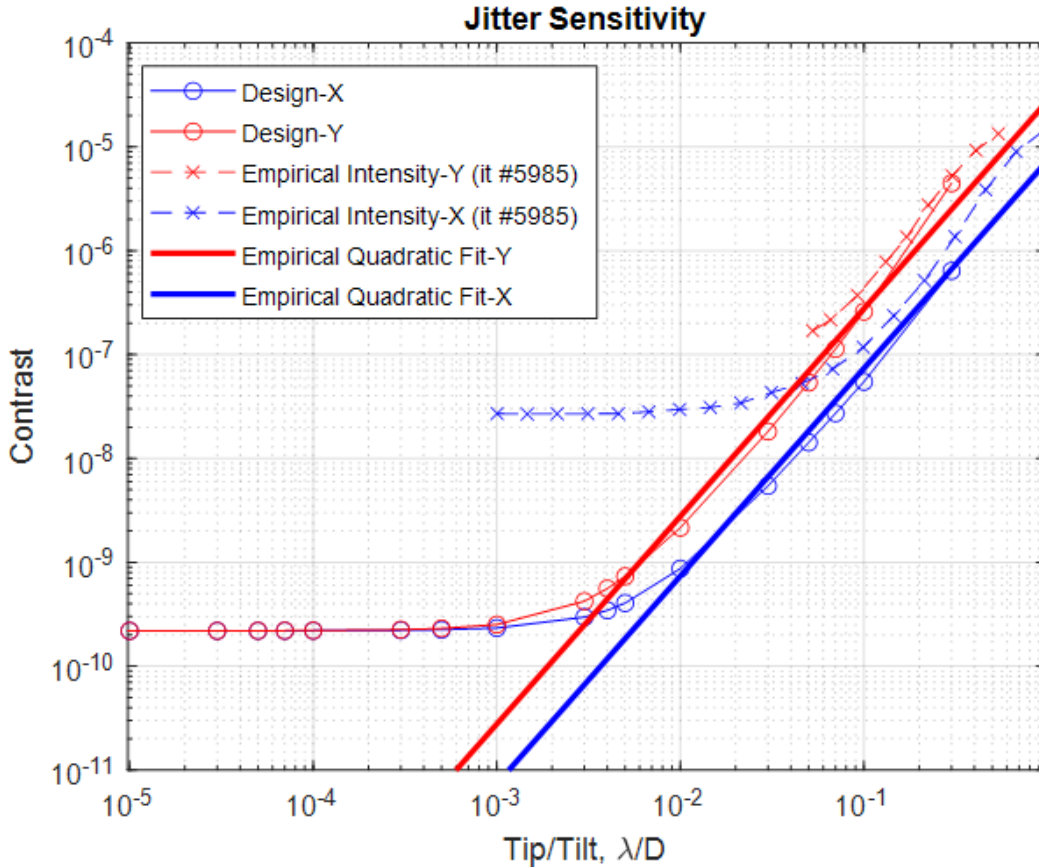


Figure 41: Measured raw mean intensity levels across the dark zone as the source displacement is increased both empirically and in the design. Also shown is the expected contrast levels from the quadratically fit jitter sensitivity as a function of tip/tilt levels.

These results show that the PIAACMC jitter sensitivity is not expected to limit contrast beyond $\sim 5e-10$ contrast inside the dark-zone, and therefore is not the limiting factor of the contrast performance in the testbed.

4.5 Preliminary analysis of limiting factors

A full analysis of limiting factors is outside the scope of this paper, but we present a few preliminary findings here. First, it is important to note that, generally speaking, the majority of a dozen or more limiting factors we encountered on the path to current performance in Figure 18 were not due to any kind of fundamental limitation of the PIAACMC technology, but rather the development of the testbed itself. It is not known yet whether the current limits are due to some kind of fundamental limitation of PIAACMC, but we have certainly not exhausted testbed and model improvements, especially in broadband light. It is therefore quite possible that, had the project gone on for longer, performance could be further improved to $\sim 1e-9$ raw contrast levels predicted by models.

A key limiting factor we were able to rule out is sensitivity to tip/tilt aberrations. Measured jitter levels on the testbed are about $0.01 \lambda/D$ rms in x and $0.0034 \lambda/D$ in y. From Figure 41, this should result in unmodulated contrast on the order of $1e-9$, well below the levels we actually observe, especially in the 2-4 λ/D dark zone. However, it is still possible that the source is not truly single mode and is acting as a star with a diameter that is too large. Another potential limiting factor is manufacturing and alignment errors. When we fold in all known errors into our models, our contrast performance stays below $1e-9$ in 10% between 2 and 8 λ/D , but there may be unknown terms on the testbed that cause limits before $1e-9$.

Other limiting factors we ruled out, or determined are not likely are: voltage resolution on the deformable mirror, most types of ghosts, chromaticity due to Fresnel diffraction, and out-of-band light present in our source. Limiting factors under investigation that are PIAACMC-related include sub-wavelength electric field interactions on the CMC mask, and polarization effects (that are not isolated by our polarizer). Ones that are not PIAACMC-related include sub-wavelength electric field interactions with the carbon nanotube pupil mask, the pinhole, DM jitter, certain types of ghosts, and insufficient software parameter tuning.

5 Conclusions

There is a significant gap between current coronagraph performance and theoretical limits, especially for obstructed apertures, which remain important because they represent a path for significant risk and cost savings on the Astro2020 mission, assuming the performance gap between coronagraphs on on-axis and off-axis apertures can be closed. PIAACMC technology is one path that may bridge both gaps, at least partially. Our PIAACMC and PIAA designs for LUVOIR show improved performance over baselined designs, especially for LUVOIR B, where the improvement in yield of characterized exoEarths is from 28 to 42. For LUVOIR A, the improvement is more modest (47 to 51), but allows new targets that are not otherwise possible. Furthermore, further improvements may be possible for obstructed apertures such as LUVOIR A, especially with the new PIAA-vortex concept.

Our current performance in the lab includes $9e-9$ raw contrast ($1.6e-9$ coherent) for a 4-8 λ/D dark zone in monochromatic light; $1.1e-7$ raw ($4.1e-8$ coherent) for 2-4 λ/D in monochromatic light; and $1.9e-8$ ($9.4e-9$ coherent) in 10% broadband light. In addition, both our design, and our empirical measurements, show tolerance to $0.02 \lambda/D$ diameter stars down to $\sim 1e-9$. Further improvements may be possible for PIAACMC, and are known to be possible for PIAA-vortex variant.

The actual limiting factor remains unknown, but we have ruled out tip/tilt sensitivity, and a number of others, such as sensitivities to known errors, voltage resolution on the deformable mirror, most types of ghosts, chromaticity due to Fresnel diffraction, and out-of-band light present in our source. Most of our prior limiting factors have been related to the development of a new testbed for PIAACMC, rather than PIAACMC itself. Although it remains possible that our limiting factor is due to some unknown fundamental limitation of the PIAACMC architecture or hardware, we have not yet exhausted possible testbed and software improvements that could have led to better performance before the testing phase of this project concluded.

6 Acknowledgements

This work was supported in part by the National Aeronautics and Space Administration's Ames Research Center, as well as the NASA Strategic Astrophysics Technology – Technology

Development for Exoplanet Missions (SAT-TDEM) program through solicitation NNH16ZDA001N-SAT at NASA's Science Mission Directorate. It was carried out at the NASA Ames Research Center, the NASA Jet Propulsion Laboratory, and the University of Arizona. Any opinions, findings, and conclusions or recommendations expressed in this article are those of the authors and do not necessarily reflect the views of the National Aeronautics and Space Administration.

References and Citations

- Belikov, R., Sirbu, D., Marx, D., Prada, C., Bendek, E., Pluzhnik, E., Bryson, S., Kern, B., Guyon, O., Fogarty, K., Knight, J., Wilson, D., Hagopian, J., "Laboratory demonstration of high contrast with the PIAACMC coronagraph on an obstructed and segmented aperture," Proc SPIE 12180 (2022).
- Belikov, R., Sirbu, D., Jewell, J., Guyon, O., Stark, C., "Theoretical performance limits for coronagraphs on obstructed and unobstructed apertures: how much can current designs be improved?," Proc SPIE 11823 (2021).
- Belikov, R., Sirbu, D., Henze, C., Stark, C., Vanderbei, R., Bendek, E., "PIAA Coronagraph Designs for Segmented Apertures, Robust to Low-Order aberrations," Proc SPIE 11117 (2019).
- Belikov, R., Bryson, S., Sirbu, D., Guyon, O., Bendek, E., Kern, B., "Design and performance analysis of a PIAACMC coronagraph on a segmented aperture," Proc SPIE 10698 (2018).
- Belikov, R., Bendek, E. A., Thomas, S., J., Males, J. R., Lozi, J., "How to directly image a habitable planet around Alpha Centauri with a ~30-45cm space telescope," *Proc SPIE* 9605-41, (2015).
- Belikov, R., Bendek, E., Greene, T.P., Guyon, O., Lozi, J., Lynch, D. H., Newman, K. E., Pluzhnik, E., Schneider, G., Tenerelli, D., Thomas, S.J., Witteborn, F. C., "EXCEDE Technology Development II: Demonstration of High Contrast at 1.2 I/D and preliminary broadband results," Proc SPIE 8864-31 (2013).
- Give'on, A., Kern, B., Shaklan, S., Moody, D.C., Pueyo, L. 2007, "Broadband wavefront correction algorithm for high-contrast imaging systems," *Proc. SPIE* **6691**, 66910A.
- Guyon, O., Martinache, F., Belikov, R., Soummer, R., "High performance PIAA coronagraphy with complex amplitude focal plane masks," *ApJS* 190, 2, pp. 220-232 (2010).
- Guyon, O., Kern, B., Belikov, R., Shaklan, S., Kuhnert, A., Give'on, A., "Phase-Induced Amplitude Apodization (PIAA) coronagraphy: recent results and future prospects," Proc SPIE 8151 (2011).
- Guyon, O., Kern, B., Kuhnert, A. 2014a, "Phase-Induced Amplitude Apodization (PIAA) Technology Development, Milestone 1: Monochromatic Contrast Demonstration," <http://exep.jpl.nasa.gov/files/exep/PIAAMilestone1.pdf>
- Guyon, O., Kern, B., Kuhnert, A. 2014b, "Phase-Induced Amplitude Apodization (PIAA) Technology Development, Milestone 3: 10% Bandpass Contrast Demonstration," <http://exep.jpl.nasa.gov/technology/Guyon-PIAA-Milestone-3.pdf>
- Guyon, O., Hinz, P.M., Cady, E., Belikov, R., Martinache, F. 2014c, "High Performance Lyot and PIAA Coronagraphy for Arbitrarily Shaped Telescope Apertures," *ApJ* **780**, 171.
- Jensen-Clem, R., Mawet, D., Gomez Gonzalez, C.A., Absil, O., Belikov, R., Currie, T., Kenworthy, M.A., Marois, C., Mazoyer, J., Ruane, G., Tanner, A., "A New Standard for Assessing the Performance of High Contrast Imaging Systems," *accepted by ApJ* (2017).
- Kern, B., Kuhnert, A., Trauger, J. 2008, "Exoplanet Exploration Coronagraph Technology: Technology Milestone #2 Report," <http://exep.jpl.nasa.gov/TPF-C/HCIT-Milestone2Signed-2008-08-08.pdf>

- Kern, B. et al. 2016, "Phase-induced amplitude apodization complex mask coronagraph mask fabrication, characterization, and modeling for WFIRST-AFTA," *J. Astron Telesc. Instrum. Syst.* **2**(1), 011014.
- Knight, M. J., Brewer, J., Hamilton, R., Ward, K., Milster, T.D., Guyon, O., "Design, fabrication, and testing of stellar coronagraphs for exoplanet imaging," *Proc. SPIE 10400* (2017).
- Krist, J. 2014, "End-to-end numerical modeling of AFTA coronagraphs," *Proc. SPIE* **9143**, 91430V.
- Krist, J., Nemati, B., Mennesson, B. 2015, "Numerical modeling of the proposed WFIRST-AFTA coronagraphs and their predicted performances," *J. Astron Telesc. Instrum. Syst.* **2**(1), 011003.
- Marx, D., Belikov, R., Sirbu, D., Kern, B., Prada, C., Bendek, E., Wilson, D., "Results from the laboratory demonstration of a PIAACMC coronagraph with a segmented aperture," *Proc SPIE 11823* (2021).
- N'Diaye, M. et al. 2016, "Apodized Pupil Lyot Coronagraphs for Arbitrary Apertures. V. Hybrid Shaped Pupil Designs for Imaging Earth-like Planets with Future Space Observatories," *ApJ* **818**, 163.
- National Academies of Sciences, Engineering, and Medicine 2021. *Pathways to Discovery in Astronomy and Astrophysics for the 2020s*. Washington, DC: The National Academies Press. <https://doi.org/10.17226/26141>.
- Newman, K., Guyon, O., Balasubramanian, K., Belikov, R., Jovanovic, N., Martinache, F., Wilson, D., "An Achromatic Focal Plane Mask for High-Performance Broadband Coronagraphy," *PASP* 127, Iss 951, pp. 437-444, (2015).
- Noecker, C. et al. 2012, "Advanced Speckle Sensing for Internal Coronagraphs," http://exep.jpl.nasa.gov/files/exep/Speckle%20Sensing%20TDEM%20Final%20Report_v12.pdf
- Riggs, A.J, et al., "High-contrast demonstration of a vector vortex coronagraph with a segmented, off-axis aperture", *SPIE Proceedings 12180*, <https://doi.org/10.1117/12.2630130> (2022).
- Seo, B.-J. et al., "Hybrid Lyot coronagraph for WFIRST: high-contrast broadband testbed demonstration", *SPIE Proceedings 10400* <https://doi.org/10.1117/12.2274687> (2017).
- Seo, B.-J. et al., "Testbed demonstration of high-contrast coronagraph imaging in search for Earth-like exoplanets", *SPIE Proceedings 11117*, <https://doi.org/10.1117/12.2530033> (2019).
- Serabyn, E. et al. 2014, "Technology Milestone #1 Report : Vortex Coronagraph Technology," http://exep.jpl.nasa.gov/technology/Serabyn_Final_2010.pdf
- Shaklan, S. et al. 2015, "Technology Milestone #1A Final Report: Coronagraph Starlight Suppression Model Validation," https://exep.jpl.nasa.gov/files/exep/COMBINEDv5_Milestone%203A%20Final%20Report%20072915.pdf
- Sirbu, D., Marx, D., Belikov, R., Bendek, E., Fogarty, K., Kern, B., Guyon, O., Pluzhnyk, E., Wilson, D., "Model validation of phase-induced amplitude apodization complex mask coronagraph for LUVOIR-A in vacuum," *Proc SPIE 11823* (2021).

Stark, C.C. et al. 2015, “Lower Limits on Aperture Size for an ExoEarth Detecting Coronagraphic Mission,” *ApJ* **808**, 149.

Trauger, J., Kern, B., Kuhnert, A. 2006, “TPF-C Technology Milestone #1 Report,” http://exep.jpl.nasa.gov/TPF-C/TPFC_M1_Report_060710_final.pdf

WFIRST milestone 3 report:

https://wfirst.gsfc.nasa.gov/science/sdt_public/wps/references/WFIRST_CGI_Milestone3_Final_Report.pdf

7 List of Acronyms

ACE	Ames Coronagraph Experiment laboratory
AFM	Atomic Force Microscope
APLC	Apodized Pupil Lyot Coronagraph
ARC	Ames Research Center
BMC	Boston Micromachines Corporation
CGH	Computer-Generated Holograph
CMC	Complex-valued Mask Coronagraph
Co-I	Co-Investigator
DM	Deformable Mirror
EFC	Electric Field Conjugation
ELT	Extremely Large Telescope
E-ELT	European Extremely Large Telescope
ExoPAG	Exoplanet Program Analysis Group
FPM	Focal Plane Mask
HabEx	Habitable Exoplanet Imaging Mission
HCIT	High Contrast Imaging Testbed
HQ	Headquarters
IWA	Inner Working Angle
JPL	Jet Propulsion Laboratory
LUVOIR	Large UltraViolet / Optical / InfraRed Surveyor
MDL	MicroDevices Laboratory
NASA	National Aeronautics and Space Administration
PI	Principal Investigator
PIAA	Phase Induced Amplitude Apodization
PIAACMC	PIAA Complex-valued Mask Coronagraph
PROPER	An optical propagation library
PSF	Point Spread Function
SCDA	Segmented Coronagraph Design & Analysis
SCExAO	Subaru Coronagraphic Extreme Adaptive Optics
SNR	Signal to Noise Ratio
SPC	Shaped Pupil Coronagraph
STDT	Science and Technology Definition Team
TAC	Technology Assessment Committee
TDEM	Technology Development for Exoplanet Missions
TPF-C	Terrestrial Planet Finder - Coronagraph
UofA	The University of Arizona
VVC	Vector Vortex Coronagraph
WFIRST	Wide Field InfraRed Survey Telescope